IOP Publishing Journal of Physics: Condensed Matter
J. Phys.: Condens. Matter **27** (2015) 245606 (17pp) doi:10.1088/0953-8984/27/24/245606

Towards a full *ab initio* theory of strong electronic correlations in nanoscale devices

David Jacob

Max-Planck-Institut für Mikrostrukturphysik, Weinberg 2, 06120 Halle, Germany

E-mail: djacob@mpi-halle.de

Received 16 April 2015
Accepted for publication 17 April 2015
Published 3 June 2015

Abstract

In this paper I give a detailed account of an *ab initio* methodology for describing strong electronic correlations in nanoscale devices hosting transition metal atoms with open d- or f-shells. The method combines Kohn–Sham density functional theory for treating the weakly interacting electrons on a static mean-field level with non-perturbative many-body methods for the strongly interacting electrons in the open d- and f-shells. An effective description of the strongly interacting electrons in terms of a multi-orbital Anderson impurity model is obtained by projection onto the strongly correlated subspace properly taking into account the non-orthogonality of the atomic basis set. A special focus lies on the *ab initio* calculation of the effective screened interaction matrix U for the Anderson model. Solution of the effective Anderson model with the one-crossing approximation or other impurity solver techniques yields the dynamic correlations within the strongly correlated subspace giving rise e.g. to the Kondo effect. As an example the method is applied to the case of a Co adatom on the Cu(0 0 1) surface. The calculated low-bias tunnel spectra show Fano–Kondo lineshapes similar to those measured in experiments. The exact shape of the Fano–Kondo feature as well as its width depend quite strongly on the filling of the Co 3d-shell. Although this somewhat hampers accurate quantitative predictions regarding lineshapes and Kondo temperatures, the overall physical situation can be predicted quite reliably.

Keywords: molecular electronics, strong correlations, Kondo effect

(Some figures may appear in colour only in the online journal)

1. Introduction

Modern experimental techniques now allow one to reliably create, manipulate and control nanoscale devices with atomic precision in the lab, thus bringing the dream of molecular electronics or nanoelectronics to create ultimately miniaturized electronic devices from single molecules closer to reality [1–4]. Prospective building blocks for molecular electronic circuits such as molecular rectifiers [5–8] and field-effect transistors [9–11] have already been demonstrated in experiments. The use of magnetic atoms or molecules promises to further enhance the functionality of molecular devices by exploiting the spin-degree of freedom of the electron in addition to its charge. Such devices could serve e.g. as basic building blocks for nanoscale spintronics applications [12, 13] or as ultimately miniaturized magnetic information storage devices [14].

Naturally, quantum effects play a crucial role in electronic devices of such tiny dimensions. Consequently, experiments with atomic- and molecular-scale devices have produced a wealth of quantum phenomena such as conductance quantization [15], quantum interference [16–19], or quantum phase transitions [20]. On the other hand, details of the atomic structure also play an important role for determining the electronic properties of nanoscale devices, especially regarding the contact between molecule and metal leads [21–23]. Also the coupling to the leads can significantly alter the electronic and magnetic properties of nanoscale devices by broadening and shifting of energy levels, as well as screening effects. Hence a proper theoretical description of nanoelectronic devices needs to take into account all of the following: quantum effects, the actual atomic structure of the device and the coupling to the leads.

The now standard approach for the description of molecular electronic devices is to combine density functional theory (DFT) calculations with the Landauer transport theory or with the non-equilibrium Green's function formalism (NEGF) [24–27]. The DFT based transport approach yields an effective mean-field description for the electronic structure and transport properties of molecular devices, taking into account quantum effects, as well as the actual atomic structure of the device, and the coupling of the device to the metallic leads. The approach works quite well for the description of metallic nanocontacts, nanowires and carbon nanotubes [21, 26, 28]. On the other hand, it was realized quite early on that this approach often overestimates conductances of molecules attached to metal leads by orders of magnitude. The origin of this was a matter of debate for about a decade [29–31]. It is now understood that this problem is largely due to DFT based transport calculations failing to produce the correct positions of the molecular energy levels by not properly capturing renormalization of molecular levels at the metal-molecule interface [32–37].

Moreover, nanoscale devices comprising magnetic atoms or molecules often display phenomena induced by so-called strong dynamic correlations that arise when the effective Coulomb interaction between the electrons exceeds their kinetic energies. Dynamic correlations can have a profound impact on the electronic and magnetic structure and the transport properties of the system. One of the most intriguing phenomena induced by dynamic correlations in nanoscale devices is probably the Kondo effect [38, 39]: Below a critical temperature characteristic of the system, the Kondo temperature T_K, the atomic or molecular spin forms a many-body singlet state with the nearby conduction electrons, thereby screening the magnetic moment of the device. The correlations usually originate from the strongly interacting open $3d$- or $4f$-shells of transition metal atoms. But also molecular orbitals of purely organic molecules only weakly coupled to the leads can give rise to strong correlations. This is corroborated by the fact that the Kondo effect is not only frequently observed in molecular devices comprising transition metal atoms [40–51], but also for devices made from purely organic molecules [42, 52–56]. By construction the DFT based transport method being a static mean-field approach cannot capture the dynamic correlations that lead e.g. to the Kondo effect in nanoscale devices[1].

Recent efforts to go beyond the DFT based transport approach are to combine time-dependent DFT (TDDFT) with the NEGF [58, 59] or the GW approximation with NEGF [60–62]. A problem of the TDDFT approach is that the standard approximations for TDDFT functionals in connection with an adiabatic exchange correlation kernel does not yield an improvement for the description of correlation effects with respect to the static DFT approach. Some progress has been made recently in that direction by finding a non-adiabatic exchange-correlation kernel for strongly correlated systems but only in the context of simplified models such as the Hubbard or Anderson model [63, 64]. The GW based transport approach on the other hand has been implemented in a fully *ab initio* way and has been applied to realistic molecular devices. GW yields an energy-dependent self-energy for describing the electronic interactions and thus captures dynamic correlation effects to some extend. Importantly, the afore mentioned problem of overestimating molecular conductances in DFT based transport calculations is solved in GW as it takes into account dynamical screening at the metal-molecule interface which leads to a proper renormalization of molecular energy levels [35]. However, GW, being perturbative in nature, does not properly account for strong electronic correlations such as those leading to the Kondo effect or the Mott–Hubbard metal–insulator transition.

Here I give a detailed account of a different *ab initio* approach for the description of strongly correlated molecular conductors which has been developed, successively refined and extended in previous work [65–69]. In this approach only the strongly interacting part of the electronic spectrum is described by advanced many-body methods in order to capture dynamic correlations effects. The weakly to moderately interacting part of the electronic system is still treated on a static mean-field level by standard Kohn–Sham DFT (KSDFT). This approach is basically an adaption of the DFT+dynamical mean-field theory (DFT+DMFT) approach [70–73], which has been developed for the realistic description of strongly correlated solids, to the special situation of nanoscale conductors. Similar approaches for treating strong correlations in molecular devices have recently appeared in the literature [74–79].

This paper is organized as follows: in section 2 a detailed account of the so far developed methodology is presented. In section 3 the methodology is applied to the case of a Co adatom at the Cu(0 0 1) surface which has been studied extensively in the recent past [80–83] and thus presents an ideal testbed for the theory. In section 4, I draw conclusions from comparison of the results to the experiments and other theoretical methods. I also discuss some of the caveats of the developed theory and possible solutions to these problems as well as future directions.

2. Methodology

The typical situations encountered in experiments with atomic and molecular devices are depicted in figure 1: (a) a magnetic molecule suspended between the tips of a metal nanocontact and (b) a magnetic atom or molecule deposited on a metallic surface probed by an STM tip. The magnetism and hence the strong correlations of the molecule are here assumed to stem from a single transition metal atom at its center. But the approach can be easily generalized to the case of multiple magnetic atoms by adaption of the dynamical mean-field theory (DMFT) to the case of molecular conductors [67]. Both situations depicted in figures 1(a) and (b) can be described by the model depicted schematically in figure 1(c): the central region, called device region D, contains the molecule or atom

[1] Recently it has been shown by Bergfield *et al* that the exact exchange correlation functional yields the exact transmission at the Fermi level in the case of the simple Anderson impurity model. However, even the exact Kohn–Sham spectrum does not yield a correct description of the spectral function and transmission outside the Fermi level. Hence the renormalization of the Kondo peak by the interactions cannot be captured by Kohn–Sham DFT based transport calculations [57].

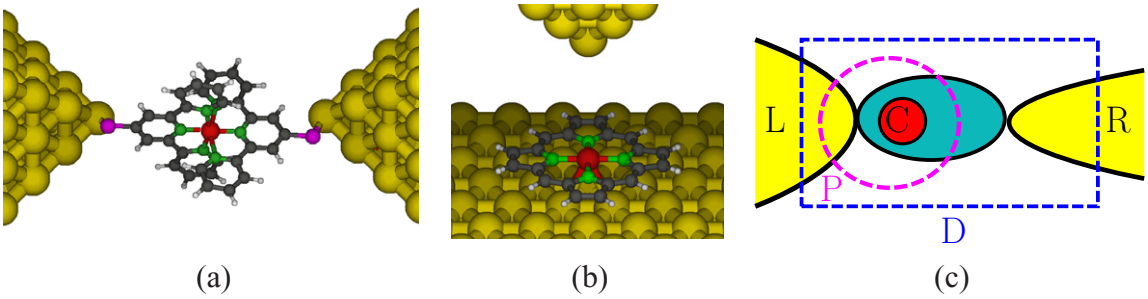

Figure 1. Typical situations encountered in molecular electronics/spintronics: (*a*) A magnetic molecule bridging the tips of a nanocontact. (*b*) A magnetic molecule on a metal surface probed by an STM tip. (*c*) Schematic sketch of model that captures both situations shown in (*a*) and (*b*). A central atom or molecule (turquoise) hosting strongly correlated levels C (red) is connected to two metal leads L and R (yellow). The device region D (blue) contains the central atom/molecule and part of the leads. The polarization region P (magenta) extends over that part of the atom/molecule and the lead(s) in close proximity to C.

and part of the leads, and will be described on the level of KSDFT. Within the atom or molecule the correlated subspace C yields the strongly interacting levels of the atom/molecule that will be treated by advanced many-body techniques in order to capture the strong dynamic correlations. The polarization region P where the polarizability is calculated in order to compute the screened interaction U of the strongly correlated subspace on the other hand extends over that part of the molecule and/or leads in immediate vicinity of the correlated subspace C. This approach can in principle also be applied directly to the case of purely organic molecules. In that case one has to identify the molecular orbitals responsible for the strong correlations [84].

The approach has been implemented within the ANT.G package [85] which interfaces the Gaussian quantum chemistry code [86] in order to implement the DFT based *ab initio* transport methodology for molecular conductors. The Gaussian code makes use of Gaussian atomic orbitals as basis sets for performing quantum chemistry and DFT calculations of finite clusters and molecules. The ANT.G package embeds the finite cluster representing the device region into bulk electrodes in order to model the transport situation depicted in figure 1. However, the formalism developed below is not specific to Gaussian basis sets. It can directly be applied to any atomic basis set, as for example the Fireball orbitals used in the SIESTA code [87]. Even more general, the formalism might be applied to any basis set as long as the different subspaces (D, P and C) can be defined in a meaningful way.

2.1. Non-orthogonal basis sets and projection onto a subspace

We now have to carefully define the projections onto the different subspaces taking into account the non-orthogonality of the atomic basis set. The choice of projection strongly influences physical quantities associated with the subspace such as the density and electronic occupancy of the subspace as has been shown recently by Soriano and Palacios [88].

We assume that the Hilbert space H of our system is spanned by a (finite) set of non-orthogonal orbitals $H = \{|\alpha\rangle\}$, i.e. $\mathrm{H} = \mathrm{span}(H)$, and $\langle\alpha|\beta\rangle = S_{\alpha\beta} \neq 0$ for $|\alpha\rangle, |\beta\rangle \in H$. We now want to project onto a subspace M of H spanned by a subset $M = \{|m\rangle\}$ of the orbitals $|\alpha\rangle \in H$, i.e. $M \subset H$. Due to the non-orthogonality of the orbitals $|\alpha\rangle \in H$, subspace M will in general have a finite overlap with the subspace R spanned by the rest of the orbitals $|r\rangle \in R \equiv H \setminus M$, i.e. $S_{mr} = \langle m|r\rangle \neq 0$ for $|m\rangle \in M$ and $|r\rangle \in R$. Hence the question arises how to define a proper projection $\hat{P}_\mathrm{M}$ onto that subspace. We note that there has actually been some controversy about this question in the literature (see e.g. [89] and references therein).

It turns out that the proper choice for $\hat{P}_\mathrm{M}$ is actually quite obvious: Let us first consider the simplest case of the subspace M being spanned by a single orbital $|m\rangle$. By definition, the projection operator for a single state is simply $\hat{P}_m = |m\rangle\langle m|$. This definition is *independent* of how (in which basis) the Hilbert space of the entire system is defined; i.e. it does not matter whether $|m\rangle$ forms part of the basis set spanning the entire Hilbert space or not; or in case it does whether it has some overlap with the Hilbert space R spanned by the rest of the basis set.

Hence it is clear that the projection $\hat{P}_\mathrm{M}$ for the subspace M can be written in an *orthonormal* basis set $M^\perp = \{|m^\perp\rangle\}$ spanning the subspace M as $\hat{P}_\mathrm{M} = \sum_{m^\perp \in M^\perp} |m^\perp\rangle\langle m^\perp|$. Such an orthonormal set can always be found by Löwdin orthogonalization of the original non-orthogonal set spanning M: $|m^\perp\rangle = \sum_m (\mathbf{S}_\mathrm{M}^{-1/2})_{mm^\perp} |m\rangle$ where $\mathbf{S}_\mathrm{M}$ is the overlap matrix between the basis set elements of M only and $\mathbf{S}_\mathrm{M}^{-1/2}$ is an abbreviation for $(\mathbf{S}_\mathrm{M})^{-1/2}$, i.e. the matrix power $-1/2$ of the matrix $\mathbf{S}_\mathrm{M}$. Hence we find for the projection operator:

$$\begin{aligned}\hat{P}_\mathrm{M} &= \sum_{m^\perp \in M^\perp} |m^\perp\rangle\langle m^\perp| \\ &= \sum_{m,n\in M} \sum_{m^\perp \in M^\perp} (\mathbf{S}_\mathrm{M}^{-1/2})_{mm^\perp} (\mathbf{S}_\mathrm{M}^{-1/2})_{m^\perp n} |m\rangle\langle n| \\ &= \sum_{m,n\in M} |m\rangle (\mathbf{S}_\mathrm{M}^{-1})_{mn} \langle n| \end{aligned} \quad (1)$$

which is nothing but the identity operator for the subspace M written in the non-orthogonal basis set. It has been argued on more formal grounds that this choice for the projection is actually the only physical reasonable one as it is the only one that leads to a tensorial consistent occupancy matrix which generates a Hermitian potential [89]. Note that the subspace projection $\hat{P}_\mathrm{M}$ defined here corresponds to the projector with regard to the Δ metric denoted by $\hat{P}_\mathrm{M}^\Delta$ in [88].

Also note that in general we cannot write the identity operator for the entire system as the sum of the projection onto subspace M and subspace R spanned by the rest of the basis set if there is some overlap between the two subspaces, i.e. $\hat{I} \neq \hat{P}_{\mathrm{M}} + \hat{P}_{\mathrm{R}}$. Rather we have to correct for the overlap between the two subspaces:

$$\hat{I} = \sum_{\alpha,\beta\in H} |\alpha\rangle (\mathbf{S}^{-1})_{\alpha\beta} \langle\beta| = \hat{P}_{\mathrm{M}} + \hat{P}_{\mathrm{R}} + \hat{O} \tag{2}$$

where $\mathbf{S}^{-1}$ is the inverse of the overlap matrix for the *entire* system. $\hat{O}$ is an operator correcting the sum of projections by the overlap between the two subspaces M and R. $\hat{P}_{\bar{\mathrm{M}}} \equiv \hat{P}_{\mathrm{R}} + \hat{O}$ defines the projection onto a new subspace $\bar{\mathrm{M}}$ which is actually orthogonal to subspace M. The projection $\hat{P}_{\bar{\mathrm{M}}}$ thus defines an orthogonalization scheme which orthogonalizes R with respect to subspace M preserving the latter.

Now let us have a look at how an operator $\hat{A}$ acting on the full Hilbert space is projected onto the subspace M:

$$\begin{aligned}\hat{A}_{\mathrm{M}} &\equiv \hat{P}_{\mathrm{M}} \hat{A} \hat{P}_{\mathrm{M}} \\ &= \sum_{m,m',n,n'\in \mathrm{M}} |m\rangle (\mathbf{S}_{\mathrm{M}}^{-1})_{mm'} \langle m'|\hat{A}|n'\rangle (\mathbf{S}_{\mathrm{M}}^{-1})_{n'n} \langle n| \\ &= \sum_{m,n\in \mathrm{M}} |m\rangle (\mathbf{S}_{\mathrm{M}}^{-1}\mathbf{A}_{\mathrm{M}}\mathbf{S}_{\mathrm{M}}^{-1})_{mn} \langle n| = \sum_{m,n\in \mathrm{M}} |m\rangle (\widetilde{\mathbf{A}}_{\mathrm{M}})_{mn} \langle n|\end{aligned} \tag{3}$$

where $\mathbf{A}_{\mathrm{M}} = (\langle m|\hat{A}|n\rangle)$ is the direct matrix given by the matrix elements of $\hat{A}$ with the basis $\{|\alpha\rangle\}$ of subspace M, and $\widetilde{\mathbf{A}}_{\mathrm{M}} = \mathbf{S}_{\mathrm{M}}^{-1}\mathbf{A}_{\mathrm{M}}\mathbf{S}_{\mathrm{M}}^{-1}$ is the so-called nuclear matrix in that basis. Note that for an orthonormal basis of M we have $\widetilde{\mathbf{A}}_{\mathrm{M}} = \mathbf{A}_{\mathrm{M}}$.

Frequently, we will also have to project an operator $\hat{A}$ given for some subspace M onto a smaller subspace $\mathrm{M}' \subset \mathrm{M}$:

$$\begin{aligned}\hat{A}_{\mathrm{M}'} &= \hat{P}_{\mathrm{M}'} \hat{A}_{\mathrm{M}} \hat{P}_{\mathrm{M}'} = \sum_{m,n\in \mathrm{M}} \hat{P}_{\mathrm{M}'}|m\rangle (\widetilde{\mathbf{A}}_{\mathrm{M}})_{\alpha\beta} \langle n|\hat{P}_{\mathrm{M}'} \\ &= \sum_{\substack{m,n\in \mathrm{M} \\ m',n',p',q'\in \mathrm{M}'}} |m'\rangle (\mathbf{S}_{\mathrm{M}'}^{-1})_{m'p'} \langle p'|m\rangle (\widetilde{\mathbf{A}}_{\mathrm{M}})_{mn} \langle n|q'\rangle (\mathbf{S}_{\mathrm{M}'}^{-1})_{q'n'} \langle n'| \\ &= \sum_{m',n'\in \mathrm{M}'} |m'\rangle (\mathbf{S}_{\mathrm{M}'}^{-1}\,\mathbf{S}_{\mathrm{M}'\mathrm{M}}\,\widetilde{\mathbf{A}}_{\mathrm{M}}\,\mathbf{S}_{\mathrm{M}\mathrm{M}'}\,\mathbf{S}_{\mathrm{M}'}^{-1})_{m'n'} \langle n'|\end{aligned} \tag{4}$$

where $\mathbf{S}_{\mathrm{M}'\mathrm{M}}$ is the overlap matrix between orbitals $|m'\rangle \in M'$ and orbitals $|m\rangle \in M$. Hence we obtain the following expression for the nuclear matrix of subspace M′ in terms of the nuclear matrix for subspace M:

$$\widetilde{\mathbf{A}}_{\mathrm{M}'} = \mathbf{S}_{\mathrm{M}'}^{-1}\,\mathbf{S}_{\mathrm{M}'\mathrm{M}}\,\widetilde{\mathbf{A}}_{\mathrm{M}}\,\mathbf{S}_{\mathrm{M}\mathrm{M}'}\,\mathbf{S}_{\mathrm{M}'}^{-1} \tag{5}$$

On the other hand, we may also have the opposite situation where we have some operator $\hat{A}_{\mathrm{M}}$ only defined on subspace M, and we want to know the direct matrix for the entire space H, i.e.

$$\langle\alpha|\hat{A}_{\mathrm{M}}|\beta\rangle = \sum_{m,n\in \mathrm{M}} \langle\alpha|m\rangle (\widetilde{\mathbf{A}}_{\mathrm{M}})_{mn} \langle n|\beta\rangle \tag{6}$$

Hence the direct matrix of the operator $\hat{A}_{\mathrm{M}}$ is given by

$$\mathbf{A}_{\mathrm{M}} = \mathbf{S}_{\mathrm{HM}}\tilde{\mathbf{A}}_{\mathrm{M}}\mathbf{S}_{\mathrm{MH}} \tag{7}$$

2.2. Projected Green's functions

The central quantities both in DFT based transport calculations of molecular electronics devices and in quantum many-body theory are Green's functions (GF). The one-body GF is defined as the resolvent of the one-body Schrödinger equation [90]:

$$\hat{G}(z)(z + \mu - \hat{H}) = \hat{I} \tag{8}$$

where z is complex, μ is the chemical potential, and $\hat{H}$ is the Hamiltonian of the system. $\hat{G}(z)$ has poles at the eigen values ϵ_k of $\hat{H}$ for a finite system or a branch cut on the real axis at the energy bands for an infinite system. Its spectral representation in terms of the eigen states $|k\rangle$ of $\hat{H}$ is given by:

$$\hat{G}(z) = (z + \mu - \hat{H})^{-1} = \sum_k \frac{|k\rangle\langle k|}{z + \mu - \epsilon_k} \tag{9}$$

The GF operator projected onto subspace M is given by:

$$\hat{G}_{\mathrm{M}}(z) = \hat{P}_{\mathrm{M}}\hat{G}(z)\hat{P}_{\mathrm{M}} = \sum_{\alpha,\beta\in M} |\alpha\rangle (\widetilde{\mathbf{G}}_{\mathrm{M}}(z))_{\alpha\beta} \langle\beta| \tag{10}$$

Defining the GF of the isolated subspace M as

$$\hat{g}_{\mathrm{M}}(z) = ((z + \mu)\hat{P}_{\mathrm{M}} - \hat{H}_{\mathrm{M}})^{-1} \tag{11}$$

and the self-energy operator $\hat{\Sigma}_{\mathrm{M}}$ associated with the coupling of the subspace M to the rest of the world as

$$\hat{\Sigma}_{\mathrm{M}}(z) = [\hat{g}_{\mathrm{M}}(z)]^{-1} - [\hat{G}_{\mathrm{M}}(z)]^{-1} \tag{12}$$

it is possible to rewrite the projected GF as

$$\hat{G}_{\mathrm{M}}(z) = \Big((z + \mu)\hat{P}_{\mathrm{M}} - \hat{H}_{\mathrm{M}} - \hat{\Sigma}_{\mathrm{M}}(z)\Big)^{-1} \tag{13}$$

The self-energy $\hat{\Sigma}_{\mathrm{M}}(z)$ is not to be confused with the one describing electron-electron interactions in the many-body GF formalism. Note that in many-body physics in the context of the Anderson impurity model [91] $\hat{\Sigma}_{\mathrm{M}}(z)$ is often called *hybridization function* and is denoted by $\hat{\Delta}_{\mathrm{M}}(z)$.

One can easily write $\hat{\Sigma}_{\mathrm{M}}(z)$ in terms of the GF for the isolated (i.e. not coupled to M) complementary space $\bar{\mathrm{M}}$ defined by $\hat{P}_{\bar{\mathrm{M}}}$, $\hat{g}_{\bar{\mathrm{M}}}(z) = ((z + \mu)\hat{P}_{\bar{\mathrm{M}}} - \hat{H}_{\bar{\mathrm{M}}})^{-1}$ as $\hat{\Sigma}_{\mathrm{M}}(z) = \hat{H}_{\mathrm{M},\bar{\mathrm{M}}}\,\hat{g}_{\bar{\mathrm{M}}}(z)\,\hat{H}_{\bar{\mathrm{M}},\mathrm{M}}$ where $\hat{H}_{\mathrm{M},\bar{\mathrm{M}}} = \hat{P}_{\mathrm{M}}\hat{H}\,\hat{P}_{\bar{\mathrm{M}}} = (\hat{H}_{\bar{\mathrm{M}},\mathrm{M}})^{\dagger}$. In order to find the matrix representations $\mathbf{G}_{\mathrm{M}}$ and $\widetilde{\mathbf{G}}_{\mathrm{M}}$ of the projected GF $\hat{G}_{\mathrm{M}}(z)$, equation (13), is multiplied with the denominator of the rhs, the matrix elements are taken and the subspace identity $\hat{P}_{\mathrm{M}}$ is inserted between the two factors of the lhs:

$$\begin{aligned}&\langle\alpha|\hat{G}_{\mathrm{M}}(z) \sum_{\alpha',\beta'\in M} |\alpha'\rangle (\mathbf{S}_{\mathrm{M}}^{-1})_{\alpha\beta'} \langle\beta'| \Big((z + \mu)\hat{P}_{\mathrm{M}} - \hat{\Sigma}_{\mathrm{M}}(z)\Big) |\beta\rangle \\ &\quad = \langle\alpha|\hat{P}_{\mathrm{M}}|\beta\rangle\end{aligned} \tag{14}$$

Hence we find for the direct GF matrix

$$\begin{aligned}\mathbf{G}_{\mathrm{M}}(z) &= \mathbf{S}_{\mathrm{M}}\left((z + \mu)\mathbf{S}_{\mathrm{M}} - \mathbf{H}_{\mathrm{M}} - \Sigma_{\mathrm{M}}(z)\right)^{-1}\mathbf{S}_{\mathrm{M}} \\ &= \left((z + \mu)\mathbf{S}_{\mathrm{M}}^{-1} - \widetilde{\mathbf{H}}_{\mathrm{M}} - \widetilde{\Sigma}_{\mathrm{M}}(z)\right)^{-1}\end{aligned} \tag{15}$$

and for the corresponding nuclear matrix

$$\widetilde{\mathbf{G}}_{\mathrm{M}}(z) = ((z + \mu)\mathbf{S}_{\mathrm{M}} - \mathbf{H}_{\mathrm{M}} - \Sigma_{\mathrm{M}}(z))^{-1} \tag{16}$$

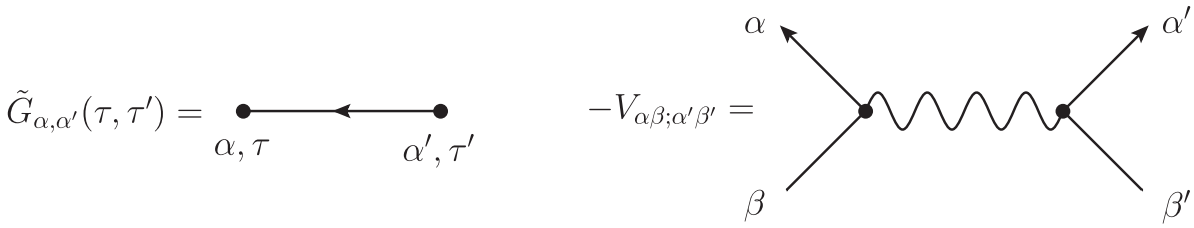

Figure 2. Feynman diagrams for the single-particle Green's function $\tilde{G}$ and the bare Coulomb interaction V_c in an atomic basis set.

2.3. Many-body Green's functions and Feynman diagrams in an atomic basis set

The generalization of the one-body Green's function for an (effectively) non-interacting system to the case of interacting electrons are the single-particle Green's function or single-particle propagators. The single-particle Matsubara GF [92] for atomic states α and α' is defined as

$$G_{\alpha\alpha'}(\tau,\tau') = -\langle T_\tau[c_\alpha(\tau), c^\dagger_{\alpha'}(\tau')]\rangle \tag{17}$$

where τ is imaginary time and the creation and annihilation operators obey the generalized anti-commutation rules for non-orthogonal basis sets [93]:

$$\{c_\alpha, c^\dagger_\beta\} = S_{\alpha\beta} \tag{18}$$

The Fourier transform with respect to imaginary time τ yields the Matsubara GF for imaginary frequencies (called Matsubara frequencies):

$$G_{\alpha\alpha'}(\mathrm{i}\omega) = \int_0^\beta \mathrm{d}\tau\, \mathrm{e}^{\mathrm{i}\omega\tau} G_{\alpha,\alpha'}(\tau,0) \tag{19}$$

By analytic continuation to the real frequency axis one obtains the retarded single-particle GF $G^{(+)}_{\alpha\alpha'}(\omega) \equiv G_{\alpha\alpha'}(\mathrm{i}\omega \to \omega + \mathrm{i}\eta)$.

$G_{\alpha\alpha'}$ defines the direct single-particle GF matrix $\mathbf{G}$. In the absence of interactions the single-particle GF matrix $\mathbf{G}$ turns out to be equal to the one-body GF matrix defined as the resolvent of the one-body Schrödinger equation. Analogous to the one-body GF we can also define the nuclear matrix for the interacting single-particle GF as $\widetilde{\mathbf{G}} = \mathbf{S}^{-1}\mathbf{G}\mathbf{S}^{-1}$.

For the development of a diagrammatic expansion for the interacting GF in a non-orthogonal basis in terms of the Coulomb interaction and the non-interacting GF, one has to either use the nuclear GF matrix in combination with the direct Coulomb interaction matrix, or the direct GF matrix in combination with the nuclear matrix of the Coulomb interaction [93]. Here we will work with the nuclear matrix for the Green's functions and the direct matrix for the interactions.

The bare Coulomb interaction in an atomic basis set is given by:

$$\mathcal{V}^{e-e} = \frac{1}{2} \sum_{\alpha,\alpha',\beta,\beta',\sigma,\sigma'} \widetilde{V}_{\alpha\beta;\alpha'\beta'}\, c^\dagger_{\alpha\sigma} c^\dagger_{\alpha'\sigma'} c_{\beta'\sigma'} c_{\beta\sigma} \tag{20}$$

where $\widetilde{V}_{\alpha\beta;\alpha'\beta'}$ is the nuclear matrix of the Coulomb interaction [93], i.e. $\widetilde{\mathbf{V}}(1,2) = \mathbf{S}(1)^{-1}\mathbf{S}(2)^{-1}\mathbf{V}(1,2)\mathbf{S}(2)^{-1}\mathbf{S}(1)^{-1}$ and the direct matrix elements are given by

$$V_{\alpha\beta;\alpha'\beta'} = e^2 \int\int \mathrm{d}r_1 \mathrm{d}r_2 \frac{\phi^*_\alpha(r_1)\phi_\beta(r_1)\phi^*_{\alpha'}(r_2)\phi_{\beta'}(r_2)}{\|r_1 - r_2\|} \tag{21}$$

The Feynman diagrams for the GF and the Coulomb interaction in an atomic basis set are shown in figure 2.

2.4. DFT based transport calculations

We consider the situation schematically depicted in figure 1(*c*). The central device region D containing a molecule is coupled to two electrodes L and R. This situation can be realized in a number of ways as shown in figures 1(*a*) and (*b*): (a) A molecule bridging the tips of a nanocontact or (b) a molecule deposited on a metal substrate and coupled to an STM tip. In addition to the molecule the device region D contains those parts of the two electrodes which are in close proximity to the molecule and whose electronic structure is modified by the presence of the molecule and vice versa. In the case of the molecular bridge (a) the tips of the nanocontact are included in the device region while in the case of the molecule on the substrate (b), part of the surface and of the STM tip are included in the device region.

The electronic structure of the central device region is calculated *ab initio* on the level of DFT in the Kohn–Sham (KS) framework, taking into account the coupling to the electrodes L and R. The Kohn–Sham Green's function of the device region D is given by:

$$\widetilde{\mathbf{G}}^0_\mathrm{D}(z) = ((z+\mu)\mathbf{S}_\mathrm{D} - \mathbf{H}^0_\mathrm{D} - \Sigma_\mathrm{L}(z) - \Sigma_\mathrm{R}(z))^{-1} \tag{22}$$

where $\mathbf{H}^0_\mathrm{D}$ is the KS Hamiltonian of the device region which yields an effective mean-field description of the electronic structure of the device region. $\mathbf{\Sigma}_\mathrm{L}(z)$ and $\mathbf{\Sigma}_\mathrm{R}(z)$ are the lead self-energies associated with the coupling of the device region to the bulk electrodes.

From the device GF the electronic density can easily be calculated by integration up to $\omega = 0$ (corresponding to the chemical potential μ)

$$\widetilde{\mathbf{D}}^0_\mathrm{D} = -\mathrm{Im}\,\frac{1}{\pi}\int_{-\infty}^0 \mathrm{d}\omega\, \widetilde{\mathbf{G}}^0_\mathrm{D}(\omega + \mathrm{i}\eta) \tag{23}$$

the density matrix yields a new KS Hamiltonian for the device region thus closing the self-consistency cycle of the KS calculation. Hence we can self-consistently calculate the electronic structure of the device region taking into account the coupling to the electrodes (open system).

In contrast to D, the electronic structure (Hamiltonian) of the electrodes L and R, and hence the self-energies are kept fixed during the self-consistent calculation of the electronic structure of D. Depending on the situation, different models for the bulk electrodes can be employed. One can for example choose nanowires [94], embed the cluster into a perfect crystalline surface calculated *ab initio* [26], or use so-called absorbing boundary conditions (ABC) [95]. Here we choose

a tight-binding Bethe lattice model [96] with realistic tight-binding parameters obtained from DFT calculations [97]. The actual choice of the electrode model is not crucial for calculations as long as the bulk electrodes are far enough away from the central scattering region, i.e. the device region is chosen big enough and contains a sufficiently big part of the electrodes [98].

Once the KS calculation is converged the transport properties can be calculated within the Landauer approach from the transmission function which is given by:

$$T^0(\omega) = \mathrm{Tr}[\mathbf{\Gamma}_\mathrm{L}(\omega)\widetilde{\mathbf{G}}^{0\dagger}_\mathrm{D}(\omega)\mathbf{\Gamma}_\mathrm{R}(\omega)\widetilde{\mathbf{G}}^{0}_\mathrm{D}(\omega)] \tag{24}$$

where $\mathbf{\Gamma}_\mathrm{L} \equiv \mathrm{i}(\mathbf{\Sigma}_\mathrm{L} - \mathbf{\Sigma}^\dagger_\mathrm{L})$ and $\mathbf{\Gamma}_\mathrm{R} \equiv \mathrm{i}(\mathbf{\Sigma}_\mathrm{R} - \mathbf{\Sigma}^\dagger_\mathrm{R})$ are the so-called coupling matrices which yield the broadening of the device region due to the coupling to the leads. From the transmission function the current and conductance can be calculated using the Landauer formula

$$I(V) = \frac{2e}{h}\int \mathrm{d}\omega\, T^0(\omega)\,(f(\omega-\mu_\mathrm{L}) - f(\omega-\mu_\mathrm{R})) \tag{25}$$

where μ_L and μ_R are the electrochemical potentials of the left and right lead, respectively, defined by the applied bias voltage $eV = \mu_\mathrm{L} - \mu_\mathrm{R}$. Note that in general the transmission function $T^0(\omega)$ also depends on the applied voltage V, i.e. $T^0 = T^0(\omega, V)$, and actually has to be calculated out of equilibrium by combining the KSDFT with the NEGF [24–26]. However, within the mean-field like KSDFT based NEGF approach the transmission is often not so strongly voltage dependent, and hence current and conductance can be approximated well by the equilibrium transmission $T^0(\omega, 0)$ at least for sufficiently small bias voltages.

In the typical situation of an STM setup (figure 1(*b*)), most of the applied bias voltage V will drop near the sharp STM tip, i.e. the electrochemical potential of the substrate remains fixed to the equilibrium one $\mu_\mathrm{sub} = \mu$ while that of the STM tip changes with the bias $\mu_\mathrm{tip} = \mu + eV$. The differential conductance for low bias at zero temperature is then directly given by the transmission function:

$$\begin{aligned} G(V) &= \frac{\partial I}{\partial V} \\ &= \frac{2e}{h} \times \frac{\partial}{\partial V}\int_0^{eV} \mathrm{d}\omega\, T^0(\omega) = \frac{2e^2}{h} \times T^0(eV) \end{aligned} \tag{26}$$

In contrast, for the situation of a molecule coupled symmetrically to two leads (figure 1(*a*)), the voltage will drop more or less symmetrically across the junction, i.e. $\mu_\mathrm{L} = \mu - eV/2$ and $\mu_\mathrm{R} = \mu + eV/2$. Hence for the conductance we obtain now

$$\begin{aligned} G(V) &= \frac{2e}{h} \times \frac{\partial}{\partial V}\int_{-eV/2}^{+eV/2} \mathrm{d}\omega\, T^0(\omega) \\ &= \frac{e^2}{h}\left[T^0\left(\frac{eV}{2}\right) + T^0\left(-\frac{eV}{2}\right)\right] \end{aligned} \tag{27}$$

In a more general situation where the coupling is neither completely symmetric nor completely asymmetric, more sophisticated modelling of the electrostatics or even a KS-NEGF calculation would be necessary in order to find the actual voltage drop.

2.5. Projection onto the correlated subspace: Anderson impurity model

Next we have to identify the strongly correlated subspace C. Usually C will be formed by the open d- or f-shells of transition metal atoms. However, also molecular orbitals of purely organic molecules such as C_{60} or carbon nanotubes weakly coupled to electrodes can show strong correlations if the effective interaction in these levels is big in comparison with the broadening due to the coupling to the leads. Our approach is completely general in this respect.

From now on we assume that the orbitals ϕ forming the subspace C are mutually orthogonal (but not necessarily orthogonal to the other orbitals in the device region). This can always be achieved by simple Löwdin orthogonalization of subspace C. However, note that often the orbitals spanning C are already mutually orthogonal. For example in the case of the atomic orbitals forming the open d- or f-shell of a transition metal atom, or in the case of molecular orbitals which are the eigenstates of the KS Hamiltonian of the molecule and hence by construction are orthogonal. In order to account for the strong correlations in subspace C an effective Coulomb interaction term

$$\hat{\mathcal{V}}^{e-e}_\mathrm{C} = \frac{1}{2}\sum_{\substack{ijkl\\ \sigma\sigma'}} U_{ik;jl}\, c^\dagger_{i\sigma} c^\dagger_{j\sigma'} c_{l\sigma'} c_{k\sigma} \tag{28}$$

is added acting on the orbitals in C. Note that $U_{ik;jl}$ is not the bare Coulomb interaction but an effective interaction which is usually much lower than the bare one due to screening processes by the conduction electrons. In the next section it is shown how to calculate $U_{ik;jl}$ *ab initio* from the DFT electronic structure. The full many-body Hamiltonian of the strongly interacting subspace C now reads:

$$\hat{\mathcal{H}}_\mathrm{C} = \hat{\mathcal{H}}^0_\mathrm{C} + \hat{\mathcal{V}}^{e-e}_\mathrm{C} \tag{29}$$

where the one-body part $\hat{\mathcal{H}}^0_\mathrm{C} = \sum_{i,j,\sigma}\langle\phi_i|\hat{H}^0_\mathrm{C}|\phi_j\rangle c^\dagger_{i\sigma} c_{j\sigma}$ is given by projection of the KS Hamiltonian $\hat{H}^0_\mathrm{D}$ onto C. However, since the Coulomb interaction has been taken into account already on a mean-field level in the Kohn–Sham Hamiltonian, we also need to subtract a double-counting correction (DCC) term:

$$\hat{H}^0_\mathrm{C} = \hat{P}_\mathrm{C}\hat{H}^0_\mathrm{D}\hat{P}_\mathrm{C} - \hat{V}^\mathrm{dc}_\mathrm{C} \tag{30}$$

Unfortunately, the DCC term $\hat{V}^\mathrm{dc}_\mathrm{C}$ is not exactly known for DFT, and several approximation schemes are used in practice [99]. Here the so-called atomic limit or fully localized limit (FLL) is employed [100], but generalized to the case of an anisotropic Coulomb repulsion $U_{ii;jj}$ [69]:

$$(V^\mathrm{dc}_\mathrm{C})_{ii} = \sum_j U_{ii;jj}\left(n_j - \frac{1}{2M_\mathrm{C}}\right) - J_\mathrm{H}\frac{N_\mathrm{C}-1}{2} \tag{31}$$

where $n_j = \langle c^\dagger_j c_j\rangle$ is the electronic occupation of orbital ϕ_j, M_C is the dimension of subspace C, J_H is the Hund's rule coupling given by the orbital-averaged exchange matrix

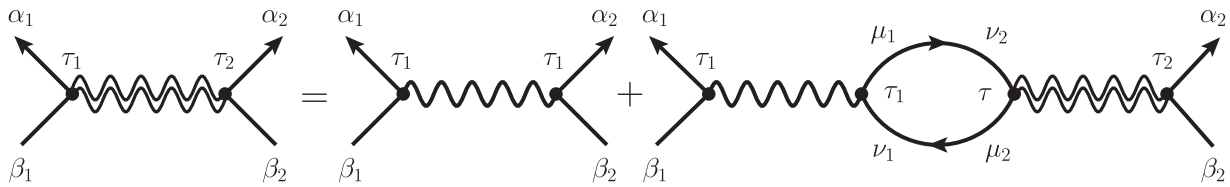

Figure 3. Dyson equation for RPA screened interaction for atomic basis set. Wiggly lines correspond to the bare Coulomb interaction V, double wiggly lines to the RPA screened interaction W.

elements $U_{ij;ji}$, and $N_C = \sum_{j\in C} n_j$ is the total electronic occupation of subspace C.

According to (16) the self-energy (a.k.a. the hybridization function) associated with the coupling of C to the rest of the system is given by

$$\Delta_C(\omega) = (\omega + \mu)\mathbf{1}_C - \mathbf{H}_C^0 - [\widetilde{\mathbf{G}}_C^0(\omega)]^{-1} \tag{32}$$

where the projected GF of the correlated subspace C ⊂ D can be calculated from the device GF according to (5) as

$$\widetilde{\mathbf{G}}_C(\omega) = \mathbf{S}_{CD}\widetilde{\mathbf{G}}_D(\omega)\mathbf{S}_{DC} \tag{33}$$

As customary in many-body physics we will call $\Delta_C(\omega)$ the hybridization function from now on. The many-body Hamiltonian $\hat{\mathcal{H}}_C$ of subspace C together with the hybridization function $\Delta_C(\omega)$ define a multi-orbital Anderson impurity model (AIM). Solution of the AIM yields the self-energy $\Sigma_C(\omega)$ describing the strong electronic correlations within the C subspace which is fed-back to the DFT calculation in order to obtain electronic spectra and transport properties of the molecular device (see section 2.8).

2.6. Computation of the effective interaction in the correlated subspace

The effective interaction $\hat{\mathcal{V}}_C^{e-e}$ between the electrons in the correlated subspace C is not the bare Coulomb interaction because of screening processes by formation of electron–hole (e–h) pairs in the rest of the system. Therefore the screened Coulomb matrix elements $U_{ik;jl}$ are considerably lower than the bare Coulomb interaction $V_{ik;jl}$. The screening of the bare interaction by formation of e–h pairs can be calculated within the so-called Random Phase Approximation (RPA) (see e.g. the book by Mahan [92] or any other textbook on quantum many-body theory). However, screening of the electrons within the C subspace will already be taken into account by the impurity solver. Hence the contribution of the impurity subspace C to the screening needs to be subtracted out. By doing so one arrives at the so-called constrained random phase approximation (cRPA) [101].

In order to calculate the effective screened interaction $U_{ik;jl}$ of subspace C within cRPA we first define the so-called polarizability region P in which screening processes due to formation of e–h pairs are taken into account for calculating the screened interaction. P comprises the strongly correlated subspace C and a sufficient portion of the surrounding atoms of subspace C as is schematically indicated in figure 1. In principle, the whole D region could be chosen as P. However, in practice this is often not feasible because of computational limitations if the device region is reasonably big. Also as it turns out the screening of the correlated subspace C by the surrounding conduction electrons is relatively localized due to the usually localized nature of the strongly correlated orbitals making up C.

Within RPA the screened interaction W is given by the Dyson equation shown diagrammatically in figure 3 which in an atomic orbital basis set can be written algebraically as

$$\begin{aligned} -W_{\alpha_1\beta_1;\alpha_2\beta_2}(\tau_1,\tau_2) &= -V_{\alpha_1\beta_1;\alpha_2\beta_2} \times \delta(\tau_1-\tau_2) \\ &- \sum_{\mu_1\nu_1\mu_2\nu_2} V_{\alpha_1\beta_1;\mu_1\nu_1} \int_0^\beta \mathrm{d}\tau\, (\widetilde{\mathbf{\Pi}}_P)_{\mu_1\nu_1;\mu_2\nu_2}(\tau_1,\tau) \\ &\times W_{\mu_2\nu_2;\alpha_2\beta_2}(\tau,\tau_2) \end{aligned} \tag{34}$$

For the screening of the bare Coulomb interaction V only screening processes within region P are taken into account. Hence we have to calculate the polarizability (i.e. the bubble diagram in figure 3) projected onto the P region:

$$(\widetilde{\mathbf{\Pi}}_P)_{\alpha\beta;\alpha'\beta'}(\tau,\tau') = \sum_\sigma (\widetilde{\mathbf{G}}_P^0)^\sigma_{\beta'\alpha}(\tau',\tau)\,(\widetilde{\mathbf{G}}_P^0)^\sigma_{\beta\alpha'}(\tau,\tau') \tag{35}$$

where the projected GF for the P region can be obtained from the device GF according to (5) as

$$\widetilde{\mathbf{G}}_P = \mathbf{S}_P^{-1}\,\mathbf{S}_{PD}\,\widetilde{\mathbf{G}}_D\,\mathbf{S}_{DP}\,\mathbf{S}_P^{-1} \tag{36}$$

For a stationary Hamiltonian we can replace the two times in the screened interaction and polarizability by time differences: $\Pi(\tau_1,\tau_2) \to \Pi(\tau_1-\tau_2)$ and $W(\tau_1,\tau_2) \to W(\tau_1-\tau_2)$. Hence (by setting $\tau_2 = 0$ and after some renaming), we can write the Dyson equation for the RPA screened interaction as:

$$\begin{aligned} W_{\alpha_1\beta_1;\alpha_2\beta_2}(\tau) &= V_{\alpha_1\beta_1;\alpha_2\beta_2} \times \delta(\tau) \\ &+ \sum_{\mu_1\nu_1\mu_2\nu_2} V_{\alpha_1\beta_1;\mu_1\nu_1} \int_0^\beta \mathrm{d}\tau'\, (\widetilde{\mathbf{\Pi}}_P)_{\mu_1\nu_1;\mu_2\nu_2}(\tau-\tau') \\ &\times W_{\mu_2\nu_2;\alpha_2\beta_2}(\tau') \end{aligned} \tag{37}$$

Here we will only consider the static limit of the screened interaction, i.e. $W^0 \equiv W(\omega=0) = \int \mathrm{d}\tau\, W(\tau)$. Because of the β-periodicity of $\Pi(\tau)$ we also have $\int_0^\beta \mathrm{d}\tau\, \Pi(\tau-\tau') = \int_0^\beta \mathrm{d}\tau\, \Pi(\tau) \equiv \Pi^0$. Hence we obtain the following Dyson equation for the *static* screened interaction W^0:

$$\begin{aligned} W^0_{\alpha_1\beta_1;\alpha_2\beta_2} &= V_{\alpha_1\beta_1;\alpha_2\beta_2} + \sum_{\mu_1\nu_1\mu_2\nu_2} V_{\alpha_1\beta_1;\mu_1\nu_1} (\widetilde{\Pi}^0_P)_{\mu_1\nu_1;\mu_2\nu_2} \\ &\times W^0_{\mu_2\nu_2;\alpha_2\beta_2} \end{aligned} \tag{38}$$

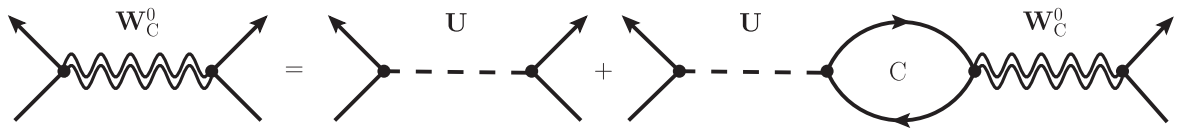

Figure 4. Dyson equation for fully screened RPA interaction $\mathbf{W}^0_{\mathrm{C}}$ of subspace C in terms of effective interaction $\mathbf{U}$. Orbital indexes have been suppressed here.

The *static* Polarizability Π^0 is now found easily by integrating a Green's function product over the frequency domain:

$$\begin{aligned}(\widetilde{\mathbf{\Pi}}^0_{\mathrm{P}})_{\mu_1\nu_1;\mu_2\nu_2} &\equiv \int_0^\beta \mathrm{d}\tau\ (\widetilde{\mathbf{\Pi}}_{\mathrm{P}})_{\mu_1\nu_1;\mu_2\nu_2}(\tau)\\ &= \int_0^\beta \mathrm{d}\tau\ \sum_\sigma (\widetilde{\mathbf{G}}^0_{\mathrm{P}})^\sigma_{\nu_2\mu_1}(-\tau)\ (\widetilde{\mathbf{G}}^0_{\mathrm{P}})^\sigma_{\nu_1\mu_2}(\tau)\\ &= \frac{1}{\beta}\sum_{\mathrm{i}\omega_n}\sum_\sigma (\widetilde{\mathbf{G}}^0_{\mathrm{P}})^\sigma_{\nu_2\mu_1}(\mathrm{i}\omega_n)\ (\widetilde{\mathbf{G}}^0_{\mathrm{P}})^\sigma_{\nu_1\mu_2}(\mathrm{i}\omega_n)\\ &\xrightarrow[\beta\to\infty]{} \frac{1}{2\pi}\int_{-\infty}^{\infty}\mathrm{d}\omega\ \sum_\sigma (\widetilde{\mathbf{G}}^0_{\mathrm{P}})^\sigma_{\nu_2\mu_1}(\omega)\ (\widetilde{\mathbf{G}}^0_{\mathrm{P}})^\sigma_{\nu_1\mu_2}(\mathrm{i}\omega)\end{aligned} \tag{39}$$

where in the last step we have taken the zero temperature limit ($\beta \to \infty$) rendering the discrete Matsubara frequencies continuous.

We now define superindices $\underline{I} := (i_1, i_2)$ in order to rewrite the Dyson equation in form of a matrix equation. Hence we have $\mathbf{W}^0 = (W^0_{\underline{I},\underline{J}})$ etc., and the Dyson equation can be written in matrix form as:

$$\mathbf{W}^0 = \mathbf{V} + \mathbf{V}\,\widetilde{\Pi}^0_{\mathrm{P}}\,\mathbf{W}^0 \tag{40}$$

Solving for the static screened interaction $\mathbf{W}^0$ we find:

$$\mathbf{W}^0 = \left(\mathbf{1} - \mathbf{V}\,\widetilde{\Pi}^0_{\mathrm{P}}\right)^{-1}\mathbf{V} \tag{41}$$

Projection to the correlated subspace C then yields the RPA screened interaction for the correlated electrons $\mathbf{W}^0_{\mathrm{C}}$. However, since the screening within the correlated subspace will already be taken into account by the impurity solver in a more or less exact way, the screening of the correlated electrons by themselves has to be subtracted out in order to obtain the effective interaction $\mathbf{U}$. Hence the effective interaction $\mathbf{U}$ is the partially screened interaction that results in the fully RPA screened interaction $\mathbf{W}^0_{\mathrm{C}}$ when taking into account only the polarizability $\widetilde{\Pi}_{\mathrm{C}}$ within the C subspace. The corresponding Dyson equation is shown diagrammatically in figure 4. Solving for the effective interaction $\mathbf{U}$ we arrive at the following 'unscreening' equation [102–104] computing $\mathbf{U}$ from $\mathbf{W}^0_{\mathrm{C}}$:

$$\mathbf{U} = \mathbf{W}^0_{\mathrm{C}}\,(\mathbf{1}_{\mathrm{C}} + \widetilde{\mathbf{\Pi}}^0_{\mathrm{C}}\mathbf{W}^0_{\mathrm{C}})^{-1} \tag{42}$$

In order to determine the screening within subspace C, we have to calculate the polarizability corresponding to subspace C.

$$\widetilde{\mathbf{\Pi}}^0_{\mathrm{C}} = \frac{1}{2\pi}\int_{-\infty}^{\infty}\mathrm{d}\omega\ \sum_\sigma (\widetilde{\mathbf{G}}_{\mathrm{C}})^\sigma_{\nu_2\mu_1}(\mathrm{i}\omega)\ (\widetilde{\mathbf{G}}_{\mathrm{C}})^\sigma_{\nu_1\mu_2}(\mathrm{i}\omega) \tag{43}$$

where $\widetilde{\mathbf{G}}_{\mathrm{C}}(\mathrm{i}\omega) = \mathbf{S}_{\mathrm{CD}}\widetilde{\mathbf{G}}_{\mathrm{D}}(\mathrm{i}\omega)\mathbf{S}_{\mathrm{DC}}$.

It is important to realize that $\widetilde{\mathbf{\Pi}}^0_{\mathrm{C}}$ and $\widetilde{\mathbf{G}}_{\mathrm{C}}$ are not just submatrices of the corresponding bigger matrices $\widetilde{\mathbf{\Pi}}^0_{\mathrm{P}}$ and $\widetilde{\mathbf{G}}_{\mathrm{P}}$ in the P region of the device due to the overlap between the subspaces. Neglecting this detail can result in serious errors in the computation of the effective Coulomb interaction $\mathbf{U}$: Due to the numerical instability of equation (42) small inaccuracies in computing $\widetilde{\mathbf{\Pi}}^0_{\mathrm{C}}$ can result in large errors and even in completely unphysical effective interactions. The numerical instability of equation (42) can be seen by rewriting it as

$$\mathbf{U} = \left(\left[\mathbf{W}^0_{\mathrm{C}}\right]^{-1} + \widetilde{\mathbf{\Pi}}^0_{\mathrm{C}}\right)^{-1} \tag{44}$$

As the fully screened interaction $\mathbf{W}^0_{\mathrm{C}}$ is usually quite small (compared to the bare Coulomb interaction) and positive, $[\mathbf{W}^0_{\mathrm{C}}]^{-1}$ is big and positive. On the other hand the screening of the correlated electrons by themselves is usually strong, and therefore $\widetilde{\mathbf{\Pi}}^0_{\mathrm{C}}$ is big and negative. Hence in order to obtain $\mathbf{U}$ we are basically subtracting two relatively big numbers and inverting the resulting small number so that relatively small errors in calculating $\mathbf{W}^0_{\mathrm{C}}$ or $\widetilde{\mathbf{\Pi}}^0_{\mathrm{C}}$ can result in quite large errors for $\mathbf{U}$. It should be noted here that in the case of a semiconducting or insulating substrate or host material, as well as in the case of insulating compounds this issue is less problematic since then at low energies around the Fermi level, the two subspaces are completely decoupled, leading to weaker 'self-screening' of the correlated electrons, and hence smaller numbers for $[\mathbf{W}^0_{\mathrm{C}}]^{-1}$ and $\widetilde{\mathbf{\Pi}}^0_{\mathrm{C}}$.

However, in the case of a metallic host or substrate considered here, it is thus crucial to correctly perform the projections of the different quantities involved in the calculation of the effective interaction (Green's functions, polarizability) to the P and C subspaces in order to reliably calculate $\mathbf{U}$. Also the usual neglect of certain product basis states in the computation of the screened interaction [105] might be problematic in this context. One way to stabilize the numerical evaluation of (42) is to decouple the correlated subspace from the rest of the system both in the calculation of $\mathbf{W}$ and of $\mathbf{U}$ as proposed by Miyake *et al* [106]. This way the self-screening of the correlated electrons is reduced considerably, leading to smaller values of $[\mathbf{W}^0_{\mathrm{C}}]^{-1}$ and $\widetilde{\mathbf{\Pi}}^0_{\mathrm{C}}$, and thus enhancing the numerical stability. However, this can lead to far too high matrix elements for the direct Coulomb interaction as will be shown in section 3. Apparently, 'mixed propagators' between the correlated subspace and the rest of the system (which vanish when the subspaces are decoupled) can be quite important for the screening of the effective interaction.

2.7. Solution of the Anderson impurity model: one-crossing approximation

Since the interaction U_{ijkl} is strong in comparison with the single-particle broadening (given by the imaginary part of

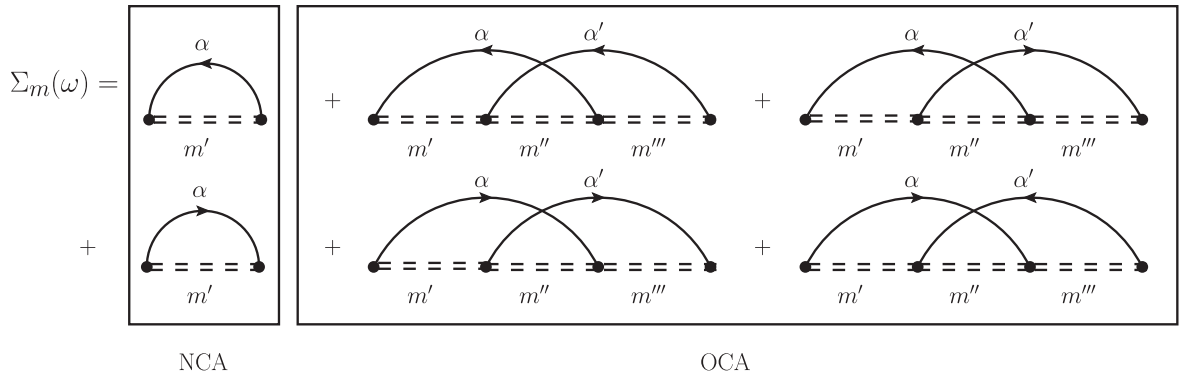

Figure 5. Diagrams for pseudo-particle self-energies in NCA and OCA approximations. Full lines correspond to conduction electron propagators coupled to impurity levels α, double dashed lines to full pseudo-particle propagators.

$\hat{\Delta}_C(\omega)$), the AIM problem cannot be solved by standard perturbation theory in the Coulomb interaction. Instead more advanced many-body methods usually starting from an exact diagonalization of the full impurity Hamiltonian $\hat{H}_C$ have to be employed in order to properly take into account the strong correlations within subspace C. Here I use the one-crossing approximation (OCA) [107] which is an improvement over the non-crossing approximation (NCA) [108–110]. However, it should be emphasized that the methodology presented so far can in principle be combined with any other method for solving the AIM, as e.g. continuous time quantum Monte-Carlo (CTQMC) [111], or numerical renormalization group (NRG) [112], or the Lanczos diagonalization scheme [76].

One advantage of OCA over other schemes is that spectral data can be calculated directly on the real frequency axis. Hence in contrast to the numerically exact CTQMC, for example, it does not suffer from artifacts introduced by numerical analytic continuation of the spectra from the Matsubara axis to the real axis. Also spurious features in the spectra coming from the approximation of the infinite and continuous conduction electron bath in the Anderson model by a finite and discrete one as in direct diagonalization schemes such as Lanczos, are not a problem for OCA since the bath is not truncated or discretized. On the other hand, in contrast to the basically exact but computationally very demanding NRG, OCA can actually be applied to realistic Anderson models of $3d$- and $4f$-impurities with 5 and 7 impurity-levels, respectively.

However, being an approximate method, OCA also suffers from some deficiencies that one should be aware of. First, as in the case of the simpler NCA, spurious non-Fermi liquid behaviour is obtained in the zero-temperature limit, resulting in artifacts in the spectral density for low temperatures. While in NCA these artifacts already appear below T_K, in OCA the critical temperature below which the artifacts appear is significantly lower (1–2 orders below T_K). Another problem of NCA and OCA is the violation of certain sum rules especially in the case of multi-orbital Anderson models that lead to errors in the high frequency expansion of the electronic self-energy [113]. Again, these errors are much less pronounced in OCA than in NCA.

The basic idea of both NCA and OCA methods is to treat the coupling of the correlated subspace C to the rest of the system given by the hybridization function $\Delta_C(\omega)$ as a perturbation to the dynamics within the subspace induced by the strong electron-electron interactions which is treated exactly. Hence the starting point is an exact diagonalization of the many-body Hamiltonian of the correlated subspace:

$$\hat{\mathcal{H}}_C = \sum_m E_m |m\rangle\langle m| \tag{45}$$

where $|m\rangle$ are the many-body eigenstates of $\mathcal{H}_C$ and E_m the corresponding eigen-energies.

It is now convenient to represent the many-body eigenstates of $|m\rangle$, in terms of auxiliary fields or *pseudo-particles* (PPs) $\hat{a}_m, \hat{a}_m^\dagger$ which obey (anti-)commutation rules depending on the number of electrons represented by the corresponding many-body state $|m\rangle$. The physical electron operators $c_{i\sigma}, c_{i\sigma}^\dagger$ are related to the PP operators by:

$$c_{i\sigma} = \sum_{m,n} F_{i\sigma}^{mn} a_m^\dagger a_n \tag{46}$$

where $F_{i\sigma}^{mn}$ are the matrix elements of the electron annihilation operator with the many-body eigenstates of C: $F_{i\sigma}^{mn} = \langle m|c_{i\sigma}|n\rangle$. Since the PPs obey (anti-)commutation rules a diagrammatic expansion of PP propagators in terms of the coupling to the rest of the system is possible. The full PP propagator corresponding to a many-body state $|m\rangle$ is then given by

$$G_m(\omega) = \frac{1}{\omega - \lambda - E_m - \Sigma_m(\omega)} \tag{47}$$

where $\Sigma_m(\omega)$ is the PP self-energy describing the dynamic interaction with the other PPs induced by the hybridization with the rest of the system (bath).

NCA consists in an infinite resummation of self-energy diagrams where conduction electron lines do not cross (hence the name). These are the diagrams shown in the left box in figure 5 for a certain PP m representing a many-body state of N electrons. The NCA diagrams describe processes where a single electron (hole) jumps from the bath to subspace C and back thereby temporarily creating a PP with $N+1$ ($N-1$) electrons. Hence the NCA self-energy is given by a convolution of the hybridization function $\Delta_C(\omega)$ with the PP propagators $G_{m'}$ of the PPs m' coupled to m. OCA additionally

takes into account diagrams where two bath electron lines cross as shown in the right box of figure 5. The algebraic expressions for the OCA self-energies involve double convolutions of two hybridization functions with three PP propagators. The exact algebraic expressions can be found in the literature [103, 107]. Since the self-energy of a PP m depends on the dressed propagators of the other PPs m' that interact via $\mathcal{V}_{\rm hyb}$ with m, the NCA/OCA equations have to be solved self-consistently.

Once the NCA/OCA equations have been solved, the real electronic quantities can be calculated from the PP propagators by expanding the real electron operators in terms of PP operators by (46). Within NCA, the real electron spectral function is obtained from the PP spectral functions as

$$\rho_{i\sigma}(\omega) = \frac{1}{\langle Q\rangle}\sum_{mm'}\int \mathrm{d}\varepsilon\, \mathrm{e}^{-\beta\varepsilon}[1+\mathrm{e}^{-\beta\omega}]|F_{i\sigma}^{mm'}|^2 \times A_m(\varepsilon)\, A_{m'}(\omega+\varepsilon) \tag{48}$$

where $A_m(\omega) = -\mathrm{Im}\, G_m(\omega)/\pi$ is the PP spectral function for PP m and Q is the PP charge which is obtained by integration of the PP spectral functions. Again. in OCA the expression for calculating the electronic density $\rho_{i\sigma}(\omega)$ is more complicated, involving double convolutions of PP spectral functions. From the electron spectral density $\rho_{i\sigma}(\omega)$ being the imaginary part (modulo π) of the electron Green's function $G_{i\sigma}(\omega)$ we can calculate the real part of $G_{i\sigma}(\omega)$ by Kramers-Kronig. Finally, from the GF $\hat{G}_{\rm C}(\omega)$ the electronic self-energy describing the dynamic correlations within C is obtained by $\hat{\Sigma}_{\rm C}(\omega) = [\hat{G}^0_{\rm C}(\omega)]^{-1} - [\hat{G}_{\rm C}(\omega)]^{-1}$ where $\hat{G}^0_{\rm C}(\omega) = ((\omega+\mu)\hat{P}_{\rm C} - \hat{H}^0_{\rm C} - \hat{\Delta}_{\rm C}(\omega))^{-1}$ is the bare propagator of subspace C. For a more detailed account of the NCA, OCA and other methods based on a hybridization expansion of atomic states see e.g. [71, 103].

2.8. Feedback of the self-energy: correlated electronic structure and transport properties

Once we have solved the Anderson impurity model for the strongly interacting subspace C coupled to the rest of the system, we obtain the electronic self-energy describing the strong dynamic correlations within subspace C:

$$\hat{\Sigma}_{\rm C}(\omega) = \sum_{i,j\in{\rm C}} |i\rangle\,[\mathbf{\Sigma}_{\rm C}(\omega)]_{ij}\,\langle j| \tag{49}$$

Note that $\widetilde{\mathbf{\Sigma}}_{\rm C} = \mathbf{\Sigma}_{\rm C}$ since we have assumed the basis to be orthonormal within subspace C. This self-energy is now fed back to the DFT part in order to obtain the correlated electronic structure and transport properties of the system. More specifically, we obtain the correlated device GF

$$\hat{G}_{\rm D}(\omega) = \left([\hat{G}^0_{\rm D}(\omega)]^{-1} - [\hat{\Sigma}_{\rm C}(\omega) - \hat{V}^{\rm dc}_{\rm C}]\right)^{-1} \tag{50}$$

where $\hat{V}^{\rm dc}_{\rm C}$ is the DCC operator which like $\hat{\Sigma}_{\rm C}(\omega)$ only acts on C. According to (7) the corresponding nuclear matrix of the device GF is

$$\widetilde{\mathbf{G}}_{\rm D}(\omega) = \left([\widetilde{\mathbf{G}}^0_{\rm D}(\omega)]^{-1} - \mathbf{S}_{\rm DC}[\mathbf{\Sigma}_{\rm C}(\omega) - \mathbf{V}^{\rm dc}_{\rm C}]\mathbf{S}_{\rm CD}\right)^{-1} \tag{51}$$

where the overlap matrices $\mathbf{S}_{\rm DC}$ and $\mathbf{S}_{\rm CD}$ sandwiching $\mathbf{\Sigma}_{\rm C}(\omega) - \mathbf{V}^{\rm dc}_{\rm C}$ account for the overlap between the correlated subspace C and the rest of the system (see equation (7)).

From the correlated device GF $\widetilde{\mathbf{G}}_{\rm D}(\omega)$ we can calculate the correlated electronic density analogously to (23) by integration of $\widetilde{\mathbf{G}}_{\rm D}(\omega)$ up to 0 energy:

$$\widetilde{\mathbf{D}}_{\rm D} = -\mathrm{Im}\,\frac{1}{\pi}\int_{-\infty}^{0}\mathrm{d}\omega\,\widetilde{\mathbf{G}}_{\rm D}(\omega+\mathrm{i}\eta) \tag{52}$$

From the correlated density in turn a new KS Hamiltonian for the device region can be calculated, from which a new correlated density is obtained and so forth until self-consistency is reached. Hence we can calculate the effect of the correlation within the C subspace onto the charge distribution of the device region. This part corresponds to the so-called 'charge self-consistency' loop within the DFT+DMFT scheme [73].

Following Meir–Wingreen [114], the low-bias transport properties can be obtained in complete analogy to the case of KS-DFT transport equations (24)–(27) even in the presence of strong correlations from the *correlated* transmission function

$$T(\omega) = \mathrm{Tr}[\mathbf{\Gamma}_{\rm L}(\omega)\widetilde{\mathbf{G}}^{\dagger}_{\rm D}(\omega)\mathbf{\Gamma}_{\rm R}(\omega)\widetilde{\mathbf{G}}_{\rm D}(\omega)] \tag{53}$$

Note that the strong correlations giving rise e.g. to the Kondo effect are actually contained in $T(\omega)$ via the correlated GF $\widetilde{\mathbf{G}}_{\rm D}(\omega)$.

In the next section we will see that the Fano–Kondo lineshapes measured by STM spectroscopy of magnetic atoms and molecules on metal substrates can indeed be reproduced by calculating the conductance from the (zero-bias) transmission function. This is due to the fact that the Kondo effect is a low-energy phenomenon, i.e. the Kondo peak is observed for very small bias voltages so that finite-bias effects only play a minor role. For the description of actual non-equilibrium phenomena the formalism has to be generalized to include the effect of finite bias voltages. As shown by Meir and Wingreen in their landmark papers [114] this can be achieved by generalization of the formalism to the Keldysh contour. However, in this case the Anderson impurity problem has to be solved out of equilibrium which is computationally extremely demanding. So far it has only been achieved in the context of the single-level AIM [115–117], but not for realistic cases.

3. Results: Co adatom at the Cu(0 0 1) surface

Now the developed methodology is applied to the case of a Co adatom deposited on the Cu(0 0 1) surface. This system is an ideal testbed for the theory as it has been measured extensively in the recent past [80, 82, 83, 118–120]. Figure 6(*a*) shows the atomic structure of the device region. The device contains the Co atom on three layers of the Cu(0 0 1) surface and an STM tip consisting of a Cu pyramid grown in the (0 0 1) direction. The Co atom and its four nearest neighbour Cu atoms have been relaxed with Gaussian09 [86] using the local spin density approximation (LSDA) and the LANL2DZ double-zeta valence plus outer core electron basis set with core pseudo potentials [121] while the rest of the device atoms have

Table 1. Total and orbital resolved occupations and spin of Co 3*d*-shell within DFT on the level of LSDA and LDA and DFT+OCA calculations.

	N_d	z^2	xz	yz	x^2-y^2	xy	S_d
LSDA	8.13	1.59	1.66	1.66	1.33	1.89	0.82
LDA	8.25	1.66	1.63	1.63	1.52	1.81	—
OCA	8.26	1.34	1.94	1.94	1.08	1.97	0.86
OCA (+0.4 eV)	8.06	1.11	1.96	1.96	1.06	1.97	0.94

Note: In the last line we show the DFT+OCA results for the Co 3*d*-levels ϵ_d shifted by 0.4 eV upwards in energy with respect to the FLL.

Table 2. Direct Coulomb repulsion matrix elements $U_{ii;kk}$ (density-density interaction) and exchange matrix elements $U_{ik;ki}$ (Hund's rule coupling) of effective Coulomb interaction for Co 3*d*-shell.

	density-density interaction (eV)					Hund's coupling (eV)			
	z^2	xz	yz	x^2-y^2	xy	z^2	xz	yz	x^2-y^2
z^2	5.38	4.27	4.27	3.45	3.46				
xz	4.27	5.56	3.86	3.73	3.74	0.60			
yz	4.27	3.86	5.56	3.73	3.74	0.60	0.83		
x^2-y^2	3.45	3.73	3.73	5.23	4.28	0.94	0.82	0.82	
xy	3.46	3.74	3.74	4.28	5.26	0.92	0.83	0.83	0.48

been kept fixed. The interlayer and intralayer distances for the fixed Cu atoms are those of a perfect Cu surface taken from [122]. In good agreement with [120, 123], I find that the Co atom relaxes at a height of about 1.5 Å above the four nearest neighbour Cu atoms while these in turn are pushed by 0.1 Å into the substrate.

Using ANT.G and the LANL2MB minimal basis set including valence and outer core electrons with pseudo potentials [121] the electronic and magnetic structure of the device coupled to the tip and substrate electrodes is calculated within DFT on the level of LSDA. The Co atom is essentially in a $4s^1 3d^8$ configuration with the two holes in the 3*d*-shell giving rise to an a approximate spin-1 state of the Co atom (see table 1) again in good agreement with [123]. LSDA basically predicts a mixed valence situation for all the orbitals with the individual occupations around 1.6 with the exception of the xy-orbital which is nearly full.

From the LSDA electronic structure the effective Coulomb interaction $U_{ij;kl}$ for the Co 3*d*-shell is calculated as described in section 2.6. For the P region we take into account substrate atoms up to the 3rd nearest neighbour, i.e. the 9 Cu atoms closest to the Co adatom. The change in U from taking into account 2nd nearest neighbours to 3rd nearest neighbours is about 2%. For 4th nearest neighbours (18 atoms in total) the super matrices in the RPA equation (41) become too big (linear matrix dimension $234^2 = 54\,756$) to be handled.

Table 2 shows the matrix elements of the effective Coulomb interaction, namely the direct Coulomb repulsion matrix elements (density-density interaction) $U_{ii;kk}$ and the exchange interaction matrix elements (Hund's rule coupling) $U_{ik;ki}$. The average density-density interaction is $\bar{U} = 4.14$ eV. It is strongly screened by the conduction electrons, resulting in a reduction of over 80% compared to the bare value of 22.9 eV for the Co 3*d*-shell. On the other hand, the Hund's rule coupling is much less affected by the screening: it is only reduced by about 10% from its bare value of 0.85 eV, resulting in an average Hund's coupling of $J_{\mathrm{H}} = 0.77$ eV. Note that the inter-orbital Coulomb repulsion ($U_{ii;kk}$ for i $\neq k$) is related to the average intra-orbital Coulomb repulsion for both orbitals and the Hund's rule coupling via $U_{ii;kk} = (U_{ii;ii} + U_{kk;kk})/2 - 2U_{ik;ki}$.

Both density-density interactions and Hund's rule coupling are somewhat anisotropic (i.e. orbital-dependent). The intra-orbital Coulomb repulsion $U_{ii;ii}$ deviates only by up to 0.17 eV or by to 3% from its mean value of $U = 5.4$ eV. The variation is stronger for the inter-orbital Coulomb repulsion $U_{ii;kk}$, deviating by up to 0.43 eV or by up to 11% from its mean value of $U' = 3.85$ eV. The Hund's rule coupling $U_{ik;ki}$ deviates even stronger by up to 0.29 eV or by up to 38% from its mean value of $J_{\mathrm{H}} = 0.77$ eV. It is worth noting at this point that the complete decoupling of the correlated subspace from the rest of the system as proposed in [106] in order to achieve a stable computation of the effective interaction in the case of 'entangled bands' produces a much higher density-density interaction of about 12 eV. Apparently the screening effects of 'mixed propagators' between the correlated subspace and the rest of the system are actually quite important and cannot be neglected.

Next, the electronic structure of the system is calculated for the paramagnetic case on the level of the local density-approximation (LDA) in order to obtain the KS energy levels of the Co 3*d*-shell ϵ_d^0 and hybridization functions $\Delta_d(\omega)$ in the absence of spin-polarization. Figure 6(b) shows the imaginary parts of the hybridization functions $\Delta_d(\omega)$ for each of the Co 3*d*-orbitals which yields the (dynamic) broadening of the orbitals due to the coupling to the substrate. We see that the broadening near the Fermi level is basically featureless indicating coupling to the delocalized Cu 4*s*-states of the substrate. As can be seen the degenerate xz- and yz-levels couple most strongly to the these states. Because of their shape these two orbitals couple very well to the 4*s*-states of the four Cu atoms directly underneath the Co adatom. On the other hand, the coupling of the xy-orbital to the substrate is the weakest for all five orbitals since the direct coupling to the

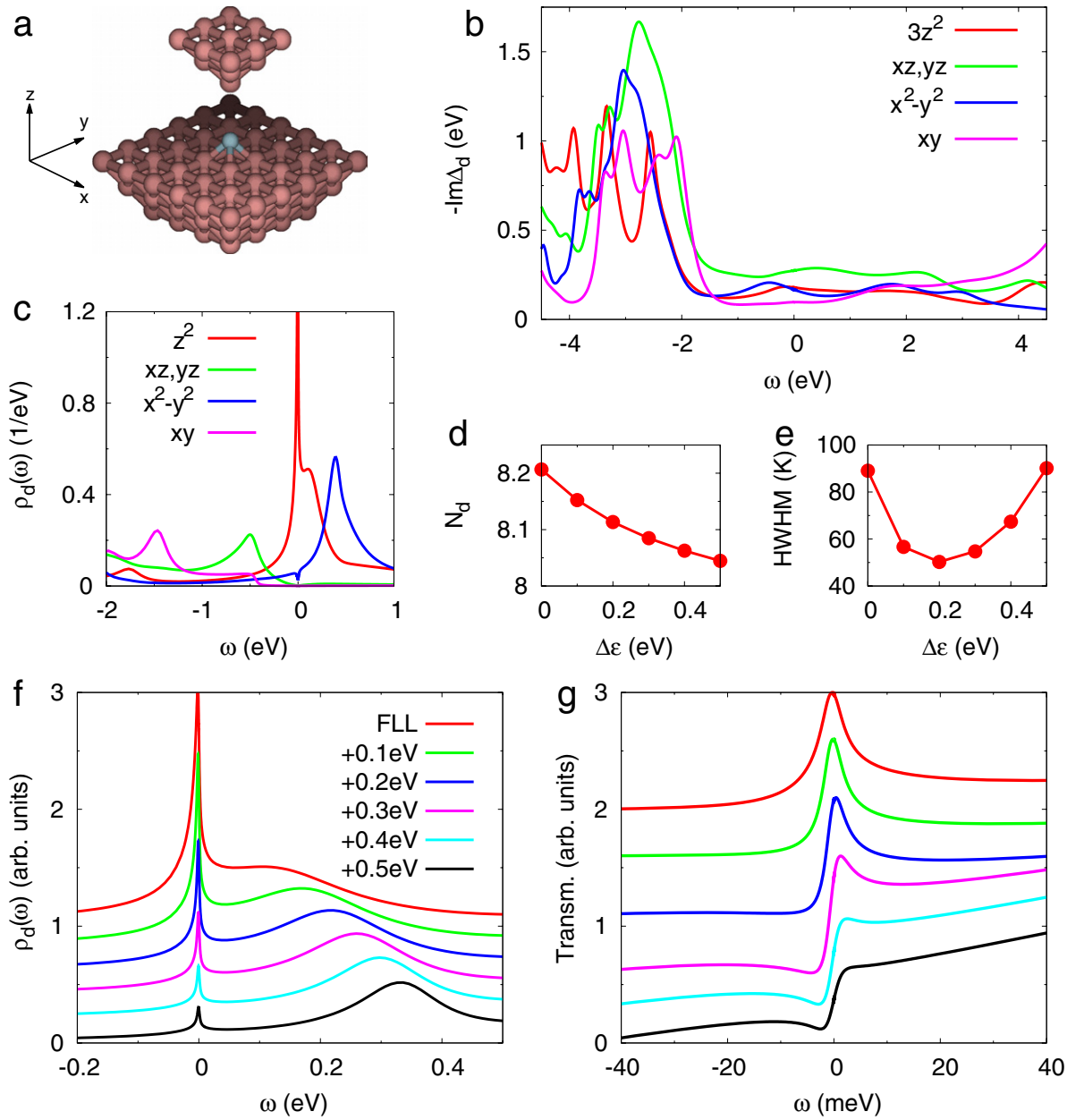

Figure 6. Results for Co adatom at Cu(0 0 1) surface. (*a*) Atomic structure of device part. The Co adatom is shown in grey. (*b*) Orbitally resolved imaginary part of hybridization functions for Co 3*d*-shell. (*c*) Orbitally resolved OCA spectral functions for Co 3*d*-shell at $T \sim 10$ K. (*d*) Total occupation of Co 3*d*-shell as a function of energy shift $\Delta\varepsilon$. (*e*) Half-width of Kondo feature in z^2 spectral function as a function of the total shift $\Delta\varepsilon$ of Co 3*d*-levels with respect to energy levels given by FLL DCC. (*f*) Spectral functions of Co z^2-orbital for different energy shifts $\Delta\varepsilon$ at $T \sim 10$ K. (*g*) DFT+OCA transmission functions for different energy shifts $\Delta\varepsilon$ (line colours as in (*f*)).

underneath Cu atoms is strongly suppressed due to symmetry reasons. The coupling of the z^2- and the $x^2 - y^2$-orbitals to the substrate is intermediate between these two cases. At negative energies, the coupling to the localized Cu 3*d*-states of the substrate leads to strong peaks in the hybridization functions at energies between -5 and -2 eV. Less pronounced peaks at positive energies above 4 eV indicate coupling to the Cu 4*p*-orbitals of the substrate.

The bare energies ϵ_d of the Co 3*d*-levels constituting the impurity shell in the Anderson impurity model are obtained from their KS energies $\epsilon_d^0 = \hat{P}_d \hat{H}^0 \hat{P}_d$ corrected by a DCC term, as explained earlier in section 2.5. The so-called FLL generalized to an anisotropic (i.e. orbital-dependent) density-density interaction $U_{ii;kk}$ is employed (31). The values for the direct Coulomb repulsion are the ones shown in table 2. For the Hund's rule coupling the orbital averaged exchange interaction is taken, i.e. $J_H = 0.77$ eV.

The Anderson impurity problem presented by the interacting Co 3*d*-shell coupled to the substrate is now solved within OCA as described in section 2.7. For the effective Coulomb interaction of the Co 3*d*-shell we take into account the density-density interactions $U_{ii;kk}$ as well as the exchange interactions $U_{ik;ki}$ as given in table 2. At the energy levels for the Co 3*d*-orbitals given by the FLL-DCC (31), the total occupancy for the Co 3*d*-shell is about 8.2 electrons similar to the ones of the LDA and LSDA calculations (see table 1).

However, the individual occupancies of the $3d$-orbitals are now quite different from the DFT ones, namely they are now closer to integer occupancies, as opposed to the mixed-valence situations obtained in the DFT calculations. In particular, the $x^2 - y^2$-orbital is now basically half-filled, and the xz-, yz- and xy-orbitals are nearly full now. The z^2-orbital is now also closer to half-filling than before but still has strong charge fluctuations (occupancy$\sim$ 1.3). Similar to LSDA, the spin of the Co $3d$-shell is found to be S_d $\sim$0.87, close to a spin-1 configuration.

In figure 6(c) the calculated spectral functions of the Co $3d$-orbitals $\rho_d(\omega)$ (at $T \sim 10$ K) are shown. We can see a very strong Kondo peak at the Fermi level in the z^2-orbital. The upper Hubbard peak is here quite close to the Kondo peak at the Fermi level due to the strong charge fluctuations. This orbital is still quite close to a mixed-valence situation. The $x^2 - y^2$-orbital despite being half-filled and thus bearing a spin-1/2 does not yield a Kondo peak. We are dealing here essentially with a so-called underscreened Kondo effect [124, 125, 126]: Despite the relatively similar hybridization of the z^2-channel and the $x^2 - y^2$-channel, the Kondo temperature T_{K,z^2} of the z^2-channel is much higher than that of the $x^2 - y^2$-channel, T_{K,x^2-y^2}, due to its stronger charge fluctuations. Hence at finite temperature T with $T_{K,x^2-y^2} < T < T_{K,z^2}$, only the spin-1/2 in the z^2-channel is Kondo-screened, while the spin-1/2 in the $x^2 - y^2$ channel remains unscreened.

The half-width of the Kondo peak is about 90 K, in very good agreement with the experimentally observed values [80, 82, 83]. However, the lineshape of the calculated transmission function (red curve in figure 6(g)) is rather peak-like, different from the experimentally observed asymmetric Fano-lineshaphes. As the DCC for DFT is not exactly known and equation (31) is only an approximation, we now shift the Co $3d$-levels upwards in energy by an amount $\Delta\varepsilon$ thus emptying the Co $3d$-shell as can be seen in figure 6(d). Emptying the Co $3d$-shell mainly lowers the occupancy of the z^2-orbital reducing the charge fluctuations for that orbital, while the occupancies of the other orbitals are quite stable. Figure 6(f) shows the effect of shifting the Co $3d$-levels and the concomitant reduction of charge fluctuations on the the spectral function of the z^2-orbital (at $T \sim 10$ K): As the z^2-orbital is emptied, its occupation approaches 1, the Kondo peak becomes smaller, and the upper Hubbard peak moves away from the Fermi level. The width of the Kondo peak decreases at first and then starts to grow again for shifts $\geqslant$0.2 eV, as can be seen in figure 6(e). Note that the non-monotonic behaviour of the width of the Kondo peak is actually a finite temperature effect: As the actual Kondo temperature decreases with decreasing charge fluctuations, the Kondo peak in the finite temperature spectra (here $T \sim 10$ K) does not attain its full (zero-temperature) height anymore. As the height of the (finite-T) Kondo peak decreases, its width starts to grow again at some point. Hence the half-width of the Kondo peak measured at some finite temperature really only yields an *apparent* Kondo temperature.

Figure 6(g) shows the effect of shifting the Co $3d$-levels on the low-energy transmission spectra. As said above, for the $3d$-levels at the values given by the FLL-DCC the transmission function near zero energy is rather peak-like, unlike the ones observed experimentally. But when shifting the $3d$-levels upwards in energy the lineshapes become more asymmetric Fano-like. Good agreement between theoretical and experimental Fano-lineshapes is achieved for shifts between 0.4–0.5 eV. In this regime the half-width of the Kondo peak is between 67 K and 86 K, in good agreement with the experimentally observed ones between 70 K and 100 K for the Co on Cu(0 0 1) system [80, 82, 83]. These results are quite different from those obtained recently for the case of Co on Cu(1 1 1) with a similar approach [127] where all the Co $3d$-orbitals give rise to Kondo-like resonances at the Fermi level. The reason could be the altogether quite different geometric situation at the (1 1 1) surface leading to a decidedly different symmetry and occupancy for the Co $3d$-shell.

4. Conclusions

In conclusion, an *ab initio* methodology has been developed for describing the impact of strong electronic correlations on the electronic structure and transport properties of nanoscale devices. Starting from the DFT electronic structure of an embedded nanoscale device, an Anderson impurity model is constructed by projection of the Kohn–Sham Hamiltonian onto the correlated subspace. The effective Coulomb interaction U for the correlated subspace (impurity) is calculated *ab initio* from the DFT electronic structure by making use of the constrained RPA approach. The solution of the Anderson impurity model yields the dynamic correlations originating from strong interactions within the correlated subspace in form of a self-energy which is fed back to the DFT calculation in order to obtain the correlated electronic structure and transport properties.

The methodology has been tested for the case of a single Co adatom on Cu(0 0 1) substrate. On a qualitative level the results are in good agreement with experiments: A Fano–Kondo feature with the width in good agreement with experiments is obtained in the calculated low-energy tunnelling spectra. However, the lineshape of the Fano–Kondo feature is not correctly reproduced at the energies for the Co $3d$-levels given by the double-counting correction. Only when shifting the Co $3d$-levels slightly upwards in energy good agreement with the experimentally observed lineshapes is achieved. It is a well known problem of DFT+U and DFT+DMFT approaches that the double-counting correction is not exactly known and in general does not yield the correct position (and thus charge) of the correlated levels. Nevertheless, the so-called fully-localized limit employed here, is actually not too far off as only moderate shifts are necessary to achieve good quantitative agreement with experiments. Importantly, the physics is actually not affected by the shifting of the Co $3d$-levels: Independent of the shift (in that energy range) the Co $3d$-shell constitutes essentially a spin-1 system that experiences an underscreened Kondo effect. The shifting only affects the weight of the Kondo peak by lowering the charge fluctuations in the Kondo-screened orbital.

Hence the developed methodology is capable of qualitative predictions of strong correlation phenomena. But

accurate quantitative predictions for example of Kondo temperatures and the exact shapes of Fano–Kondo features are difficult as these are dependent on the exact occupancy of the correlated subspace which cannot be calculated accurately because of the approximate nature of the double-counting correction in our approach. One possibility to overcome these difficulties is to make use of the GW approach instead of DFT for the description of the weakly interacting part of the system, similar to the GW+DMFT approach for strongly correlated materials [128–130] since for GW the double-counting correction term is exactly known.

Acknowledgments

I would like to thank J Palacios and M Soriano for fruitful discussions about projections in non-orthogonal basis sets, and S Biermann and K Haule for stimulating discussions on the calculation of the effective interaction U. I am also grateful to Hardy Gross for his support and encouragement.

References

[1] Heath J R and Ratner A R 2003 Molecular electronics *Phys. Today* **56** 43
[2] Joachim C and Ratner M A 2005 Molecular electronics: some views on transport junctions and beyond *Proc. Natl Acad. Sci. USA* **102** 8801
[3] Cuniberti G, Fagas G and Richter K 2005 *Introducing Molecular Electronics* (Berlin: Springer)
[4] Cuevas J C and Scheer E 2010 *Molecular Electronics* (Singapore: World Scientific)
[5] Aviram A and Ratner M A 1974 Molecular rectifiers *Chem. Phys. Lett.* **29** 277
[6] Elbing M, Ochs R, Koentopp M, Fischer M, von Hnisch C, Weigend F, Evers F, Weber H B and Mayor M 2005 A single-molecule diode *Proc. Natl Acad. Sci.* **102** 8815
[7] Díez-Pérez I, Hihath J, Lee Y, Yu L, Adamska L, Kozhushner M A, Oleynik I I and Tao N 2009 Rectification and stability of a single molecular diode with controlled orientation *Nat. Chem.* **1** 635
[8] Batra A, Darancet P, Chen Q, Meisner J S, Widawsky J R, Neaton J B, Nuckolls C and Venkataraman L 2013 Tuning rectification in single-molecular diodes *Nano Lett.* **13** 6233
[9] Tans S J, Verscheren A R M and Dekker C 1998 Room-temperature transistor based on single carbon nanotube *Nature* **393** 49
[10] Martel R, Schmidt T, Shea H R, Hertel T and Avouris Ph 1998 Single- and multi-wall carbon nanotube field-effect transistors *Appl. Phys. Lett.* **73** 2447
[11] Song H, Kim Y, Jang Y H, Jeong H, Reed M A and Lee H 2009 Observation of molecular orbital gating *Nature* **462** 1039
[12] Žutić I and Das Sarma S 2004 Spintronics: fundamentals and applications *Rev. Mod. Phys.* **76** 323
[13] Bogani L and Wernsdorfer W 2008 Molecular spintronics using single-molecule magnets *Nat. Mater.* **7** 179
[14] Gatteschi D, Sessoli R and Villain J 2006 *Molecular Nanomagnets* (Oxford: Oxford University Press)
[15] Agraït N, Yegati A L and van Ruitenbeek J M 2003 Quantum properties of atomic-sized conductors *Phys. Rep.* **377** 81
[16] Liang W, Bockrath M, Bozovic D, Hafner J H, Tinkham M and Park H 2001 Fabry–Perot interference in a nanotube electron waveguide *Nature* **411** 665
[17] Kong J, Yenilmez E, Tombler T W, Kim W, Dai H, Laughlin R B, Liu L, Jayanthi C S and Wu S Y 2001 Quantum interference and ballistic transmission in nanotube electron waveguides *Phys. Rev. Lett.* **87** 106801
[18] Aradhya S V, Meisner J S, Krikorian M, Ahn S, Parameswaran R, Steigerwald M L, Nuckolls C and Venkataraman L 2012 Dissecting contact mechanics from quantum interference in single-molecule junctions of Stilbene derivatives *Nano Lett.* **12** 1643
[19] Guédon C M, Valkenier H, Markussen T, Thygesen K S, Hummelen J C and van der Molen S J 2012 Observation of quantum interference in molecular charge transport *Nat. Nanotechnol.* **7** 305
[20] Roch N, Florens S, Bouchiat V, Wernsdorfer W and Balestro F 2008 Quantum phase transitions in a single-molecule quantum dot *Nature* **453** 633
[21] Palacios J J, Pérez-Jiménez A J, Louis E, SanFabián E and Vergés J A 2003 First-principles phase-coherent transport in metallic nanotubes with realistic contacts *Phys. Rev. Lett.* **90** 106801
[22] Palacios J J, Tarakeshwar P and Kim D M 2008 Metal contacts in carbon nanotube field-effect transistors: beyond the Schottky barrier paradigm *Phys. Rev.* B **77** 113403
[23] Schull G, Frederiksen T, Brandbyge M and Berndt R 2009 Passing current through touching molecules *Phys. Rev. Lett.* **103** 206803
[24] Taylor J, Guo H and Wang J 2001 *Ab initio* modeling of quantum transport properties of molecular electronic devices *Phys. Rev.* B **63** 245407
[25] Palacios J J, Pérez-Jiménez A J, Louis E, SanFabián E and Vergés J A 2002 First-principles approach to electrical transport in atomic-scale nanostructures *Phys. Rev.* B **66** 035322
[26] Brandbyge M, Mozos J L, Ordejón P, Taylor J and Stokbro K 2002 Density functional method for nonequilibrium electron transport *Phys. Rev.* B **65** 165401
[27] Rocha A R, Garcia-Suarez V M, Bailey S, Lambert C, Ferrer J and Sanvito S 2006 Spin and molecular electronics in atomically generated orbital landscapes *Phys. Rev.* B **73** 085414
[28] Mehrez H, Wlasenko A, Larade B, Taylor J, Grütter P and Guo H 2002 I–V characteristics and differential conductance fluctuations of Au nanowires *Phys. Rev.* B **65** 195419
[29] Di Ventra M, Pantelides S T and Lang N D 2000 First-principles calculation of transport properties of a molecular device *Phys. Rev. Lett.* **84** 979
[30] Varga K and Pantelides S T 2007 Quantum transport in molecules and nanotube devices *Phys. Rev. Lett.* **98** 076804
[31] Lindsay S M and Ratner M A 2007 Molecular transport junctions: clearing mists *Adv. Mater.* **19** 23
[32] Thygesen K S and Rubio A 2009 Renormalization of molecular quasiparticle levels at metal-molecule interfaces: trends across binding regimes *Phys. Rev. Lett.* **102** 046802
[33] Mera H and Niquet Y M 2010 Are Kohn–Sham conductances accurate? *Phys. Rev. Lett.* **105** 216408
[34] Dell M *et al* 2010 Relating energy level alignment and amine-linked single molecule junction conductance *Nano Lett.* **10** 2470
[35] Strange M, Rostgaard C, Häkkinen H and Thygesen K S 2011 Self-consistent gw calculations of electronic transport in thiol- and amine-linked molecular junctions *Phys. Rev.* B **83** 115108
[36] Tamblyn I, Darancet P, Quek S Y, Bonev S A and Neaton J B 2011 Electronic energy level alignment at metal-molecule interfaces with a *GW* approach *Phys. Rev.* B **84** 201402
[37] Strange M and Thygesen K S 2012 Image-charge-induced localization of molecular orbitals at metal-molecule

interfaces: self-consistent *GW* calculations *Phys. Rev.* B **86** 195121
[38] Kondo J 1964 Resistance minimum in dilute magnetic alloys *Prog. Theor. Phys.* **32** 37
[39] Hewson A C 1993 *The Kondo problem to heavy fermions* (Cambridge: Cambridge University Press)
[40] Madhavan V, Chen W, Jamneala T, Crommie M F and Wingreen N S 1998 Tunneling into a single magnetic atom: spectroscopic evidence of the kondo resonance *Science* **280** 567
[41] Li J, Schneider W-D, Berndt R and Delley B 1998 Kondo scattering observed at a single magnetic impurity *Phys. Rev. Lett.* **80** 2893
[42] Park J *et al* 2002 Coulomb blockade and Kondo effect in single-atom transistors *Nature* **417** 722
[43] Liang W, Shores M P, Bockrath M, Long J R and Park H 2002 Kondo resonance in a single-molecule transistor *Nature* **417** 729
[44] Zhao A *et al* 2005 Controlling the Kondo effect of an adsorbed magnetic ion through its chemical bonding *Science* **309** 1542
[45] Yu L H, Keane Z K, Ciszek J W, Cheng L, Tour J M, Baruah T, Pederson M R and Natelson D 2005 Kondo resonances and anomalous gate dependence in the electrical conductivity of single-molecule transistors *Phys. Rev. Lett.* **95** 256803
[46] Iancu V, Deshpande A and Hla S-W 2006 Manipulating Kondo temperature via single molecule switching *Nano Lett.* **6** 820
[47] Fu Y-S *et al* 2007 Manipulating the Kondo resonance through quantum size effects *Phys. Rev. Lett.* **99** 256601
[48] Calvo M R, Fernández-Rossier J, Palacios J J, Jacob D, Natelson D and Untiedt C 2009 The Kondo effect in ferromagnetic atomic contacts *Nature* **358** 1150
[49] Franke K J, Schulze G and Pacual J I 2011 Competition of superconducting phenomena and Kondo screening at the nanoscale *Science* **332** 940
[50] Minamitani E, Tsukahara N, Matsunaka D, Kim Y, Takagi N and Kawai M 2012 Symmetry-driven novel Kondo effect in a molecule *Phys. Rev. Lett.* **109** 086602
[51] Kügel J, Karolak M, Senkpiel J, Hsu P-J, Sangiovanni G and Bode M 2014 Relevance of hybridization and filling of 3d orbitals for the Kondo effect in transition metal phthalocyanines *Nano Lett.* **14** 3895
[52] Nygard J, Cobden D H and Lindelof P E 2000 Kondo physics in carbon nanotubes *Nature* **408** 342
[53] Yu L H and Natelson D 2004 The Kondo effect in C_60 single-molecule transistors *Nano Lett.* **4** 79
[54] Jarillo-Herrero P, Kong J, van der Zant H S J, Dekker C, Kouwenhoven L P and De Franceschi S 2005 Orbital Kondo effect in carbon nanotubes *Nature* **434** 484
[55] Parks J J, Champagne A R, Hutchison G R, Flores-Torres S, Abruña H D and Ralph D C 2007 Tuning the Kondo effect with a mechanically controllable break junction *Phys. Rev. Lett.* **99** 026601
[56] Roch N, Florens S, Costi T A, Wernsdorfer W and Balestro F 2009 Observation of the underscreened Kondo effect in a molecular transistor *Phys. Rev. Lett.* **103** 197202
[57] Bergfield J P, Liu Z-F, Burke K and Stafford C A 2012 Bethe ansatz approach to the Kondo effect within density-functional theory *Phys. Rev. Lett.* **108** 066801
[58] Stefanucci G and Almbladh C-O 2004 Time-dependent partition-free approach in resonant tunneling systems *Phys. Rev.* B **69** 195318
[59] Di Ventra M and Todorov T N 2004 Transport in nanoscale systems: the microcanonical versus grand-canonical picture *J. Phys.: Condens. Matter* **16** 8025
[60] Darancet P, Ferretti A, Mayou D and Olevano V 2007 *Ab initio* GW electron–electron interaction effects in quantum transport *Phys. Rev.* B **75** 075102
[61] Thygesen K S and Rubio A 2007 Non-equilibrium GW approach to quantum transport in nanoscale contacts *J. Chem. Phys.* **126** 091101
[62] Darancet P, Widawsky J R, Choi H J, Venkataraman L and Neaton J B 2012 Quantitative current-voltage characteristics in molecular junctions from first principles *Nano Letters* **12** 6250 PMID: 23167709
[63] Stefanucci G and Kurth S 2011 Towards a description of the Kondo effect using time-dependent density-functional theory *Phys. Rev. Lett.* **107** 216401
[64] Turkowski V and Rahman T S 2014 Nonadiabatic time-dependent spin-density functional theory for strongly correlated systems *J. Phys.: Condens. Matter* **26** 022201
[65] Jacob D, Haule K and Kotliar G 2009 Kondo effect and conductance of nanocontacts with magnetic impurities *Phys. Rev. Lett.* **103** 016803
[66] Jacob D and Kotliar G 2010 Orbital selective and tunable Kondo effect of magnetic adatoms on graphene: correlated electronic structure calculations *Phys. Rev.* B **82** 085423
[67] Jacob D, Haule K and Kotliar G 2010 Dynamical mean-field theory for molecular electronics: electronic structure and transport properties *Phys. Rev.* B **82** 195115
[68] Karolak M, Jacob D and Lichtenstein A I 2011 Orbital Kondo effect in cobalt-benzene sandwich molecules *Phys. Rev. Lett.* **107** 146604
[69] Jacob D, Soriano M and Palacios J J 2013 Kondo effect and spin quenching in high-spin molecules on metal substrates *Phys. Rev.* B **88** 134417
[70] Anisimov V, Poteryaev A, Korotin M, Anokhin A and Kotliar G 1997 First-principles calculations of the electronic structure and spectra of strongly correlated systems: dynamical mean-field theory *J. Phys.: Condens. Matter* **9** 7359
[71] Kotliar G, Savrasov S Y, Haule K, Oudovenko V S, Parcollet O and Marianetti C A 2006 Electronic structure calculations with dynamical mean-field theory: a spectral density functional approach *Rev. Mod. Phys.* **78** 865
[72] Karolak M, Wehling T O, Lechermann F and Lichtenstein A I 2011 General DFT++ method implemented with projector augmented waves: electronic structure of $SrVO_3$ and the mott transition in $Ca_{2-x}Sr_xRuO_4$ *J. Phys.: Condens. Matter* **23** 085601
[73] Pourovskii L, Amadon B, Biermann S and Georges A 2007 Self-consistency over the charge density in dynamical mean-field theory: a linear muffin-tin implementation and some physical implications *Phys. Rev.* B **76** 235101
[74] Dias da Silva L G G V, Tiago M L, Ulloa S E, Reboredo F A and Dagotto E 2009 Many-body electronic structure and Kondo properties of cobalt-porphyrin molecules *Phys. Rev.* B **80** 155443
[75] Korytár R and Lorente N 2011 Multi-orbital non-crossing approximation from maximally localized wannier functions: the Kondo signature of copper phthalocyanine on Ag(1 0 0) *J. Phys.: Condens. Matter* **23** 355009
[76] Ishida H and Liebsch A 2012 Coulomb blockade and Kondo effect in the electronic structure of hubbard molecules connected to metallic leads: a finite-temperature exact-diagonalization study *Phys. Rev.* B **86** 205115
[77] Valli A, Sangiovanni G, Toschi A and Held K 2012 Correlation effects in transport properties of interacting nanostructures *Phys. Rev.* B **86** 115418
[78] Ryndyk D A, Donarini A, Grifoni M and Richter K 2013 Many-body localized molecular orbital approach to molecular transport *Phys. Rev.* B **88** 085404

[79] Baruselli P P, Fabrizio M, Smogunov A, Requist R and Tosatti E 2013 Magnetic impurities in nanotubes: from density functional theory to Kondo many-body effects *Phys. Rev.* B **88** 245426

[80] Knorr N, Schneider M A, Diekhöner L, Wahl P and Kern K 2002 Kondo effect of single Co adatoms on Cu surfaces *Phys. Rev. Lett.* **88** 096804

[81] Wahl P, Diekhöner L, Wittich G, Vitali L and Schneider M A 2005 Kondo effect of molecular complexes at surfaces: ligand control of the local spin couppling *Phys. Rev. Lett.* **95** 166601

[82] Néel N, Kröger J, Limot L, Palotas K, Hofer W A and Berndt R 2007 Conductance and Kondo effect in a controlled single-atom contact *Phys. Rev. Lett.* **98** 016801

[83] Uchihashi T, Zhang J, Kröger J and Berndt R 2008 Quantum modulation of the Kondo resonance of Co adatoms on Cu/Co/Cu(1 0 0): low-temperature scanning tunneling spectroscopy study *Phys. Rev.* B **78** 033402

[84] Soriano M, Jacob D and Palacios J J in preparation

[85] Palacios J J, Jacob D, Pérez-Jiménez A J, San Fabián E, Louis E and Vergés J A ANT.G: Atomistic Nano Transport with Gaussian http://antgaussian.sourceforge.net

[86] Frisch M J *et al* 2009 Gaussian09 Revision D.01. Gaussian Inc. Wallingford CT

[87] Soler J M, Artacho E, Gale J D, García A, Junquera J, Ordejón P and Sánchez-Portal D 2002 The SIESTA method for *ab initio* order-N materials simulation *J. Phys.: Condens. Matter* **14** 2745

[88] Soriano M and Palacios J J 2014 Theory of projections with nonorthogonal basis sets: partitioning techniques and effective Hamiltonians *Phys. Rev.* B **90** 075128

[89] O'Regan D D, Payne M C and Mostofi A A 2011 Subspace representations in *ab initio* methods for strongly correlated systems *Phys. Rev.* B **83** 245124

[90] Economou E N 1970 *Green's functions in Quantum Physics* (*Springer Series in Solid State Physics*) (Berlin: Springer)

[91] Anderson P W 1961 Localized magnetic states in metals *Phys. Rev.* **124** 41

[92] Mahan G D 2000 *Many-Particle Physics* 3rd edn (New York: Plenum)

[93] Thygesen K S 2006 Electron transport through an interacting region: the case of a nonorthogonal basis set *Phys. Rev.* B **73** 035309

[94] Taylor J, Guo H and Wang J 2001 *Ab initio* modeling of open systems: charge transfer, electron conduction, and molecular switching of a C_{60} device *Phys. Rev.* B **63** 121104

[95] Baer R, Seideman T, Ilani S and Neuhauser D 2004 *Ab initio* study of the alternating current impedance of a molecular junction *J. Chem. Phys.* **120** 3387

[96] Palacios J J, Pérez-Jiménez A J, Louis E, SanFabián E, Vergés J A and García Y 2005 Molecular electronics with Gaussian98/03 *Computational Chemistry: Reviews of Current Trends* vol 9 ed J Leszczynski (Singapore: World Scientific)

[97] Papaconstantopoulos D A 1986 *Handbook of the Band Structure of Elemental Solids* (New York: Plenum)

[98] Jacob D and Palacios J J 2011 Critical comparison of electrode models in density functional theory based quantum transport calculations *J. Chem. Phys.* **134** 044118

[99] Karolak M, Ulm G, Wehling T O, Mazurenko V, Poteryaev A and Lichtenstein A 2010 Double counting in LDA+DMFT—the example of NiO *J. Electron Spectrosc. Relat. Phenom.* **181** 11

[100] Czyzyk M T and Sawatzky G A 1994 Local density functional and on-site correlations: the electronic structure of La_2CuO_4 and $LaCuO_3$ *Phys. Rev.* B **49** 14211

[101] Aryasetiawan F, Karlsson K, Jepsen O and Schonberger U 2006 Calculations of Hubbard U from first-principles *Phys. Rev.* B **74** 125106

[102] Aryasetiawan F, Imada M, Georges A, Kotliar G, Biermann S and Lichtenstein A I 2004 Frequency-dependent local interactions and low-energy effective models from electronic structure calculations *Phys. Rev.* B **70** 195104

[103] Kutepov A, Haule K, Savrasov S Y and Kotliar G 2010 Self-consistent GW determination of the interaction strength: application to the iron arsenide superconductors *Phys. Rev.* B **82** 045105

[104] Vaugier L, Jiang H and Biermann S 2012 Hubbard U and hund exchange J in transition metal oxides: screening versus localization trends from constrained random phase approximation *Phys. Rev.* B **86** 165105

[105] Aryasetiawan F and Gunnarsson O 1998 The GW method *Rep. Prog. Phys.* **61** 237

[106] Miyake T, Aryasetiawan F and Imada M 2009 *Ab initio* procedure for constructing effective models of correlated materials with entangled band structure *Phys. Rev.* B **80** 155134

[107] Haule K, Kirchner S, Kroha J and Wölfle P 2001 Anderson impurity model at finite coulomb interaction U: generalized noncrossing approximation *Phys. Rev.* B **64** 155111

[108] Grewe N and Keiter H 1981 Diagrammatic approach to the intermediate-valence compounds *Phys. Rev.* B **24** 4420

[109] Kuramoto Y 1983 Self-consistent perturbation theory for dynamics of valence fluctuations *Z. Phys.* B **53** 37

[110] Coleman P 1984 New approach to the mixed-valence problem *Phys. Rev.* B **29** 3035

[111] Gull E, Millis A J, Lichtenstein A I, Rubtsov A N, Troyer M and Werner P 2011 Continuous-time Monte Carlo methods for quantum impurity models *Rev. Mod. Phys.* **83** 349

[112] Bulla R, Costi T A and Pruschke Th 2008 Numerical renormalization group method for quantum impurity systems *Rev. Mod. Phys.* **80** 3950

[113] Rüegg A, Gull E, Fiete G A and Millis A J 2013 Sum rule violation in self-consistent hybridization expansions *Phys. Rev.* B **87** 075124

[114] Meir Y and Wingreen N S 1992 Landauer formula for the current through an interacting electron region *Phys. Rev. Lett.* **68** 2512

[115] Meir Y, Wingreen N S and Lee P A 1993 Low-temperature transport through a quantum dot: the Anderson model out of equilibrium *Phys. Rev. Lett.* **70** 2601

[116] Wingreen N S and Meir Y 1994 Anderson model out of equilibrium: noncrossing-approximation approach to transport through a quantum dot *Phys. Rev.* B **49** 11040

[117] Cohen G, Gull E, Reichman D R and Millis A J 2014 Green's functions from real-time bold-line Monte Carlo calculations: spectral properties of the nonequilibrium anderson impurity model *Phys. Rev. Lett.* **112** 146802

[118] Wahl P, Diekhöner L, Schneider M A, Vitali L, Wittich G and Kern K 2004 Kondo temperature of magnetic impurities at surfaces *Phys. Rev. Lett.* **93** 176603

[119] Neél N, Kröger J, Berndt R, Wehling T, Lichtenstein A and Katsnelson M I 2008 Controlling the Kondo effect in $CoCu_n$ clusters atom by atom *Phys. Rev. Lett.* **101** 266803

[120] Vitali L, Ohmann R, Stepanow S, Gambardella P, Tao K, Huang R, Stepanyuk V, Bruno P and Kern K 2008 Kondo effect in single atom contacts: the importance of the atomic geometry *Phys. Rev. Lett.* **101** 216802

[121] Hay P J and Wadt W R 1985 *Ab initio* effective core potentials for molecular calculations—potentials for K to Au including the outermost core orbitals *J. Chem. Phys.* **82** 299

[122] Da Silva J, Schroeder K and Blügel S 2004 First-principles investigation of the multilayer relaxation of stepped Cu surfaces *Phys. Rev.* B **69** 245411

[123] Pick Š, Stepanyuk V, Baranov A, Hergert W and Bruno P 2003 Effect of atomic relaxations on magnetic properties of adatoms and small clusters *Phys. Rev.* B **68** 104410

[124] Noziéres Ph and Blandin A 1980 Kondo effect in real metals *J. Phys.* **41** 193

[125] Coleman P and Pépin C 2003 Singular Fermi liquid behavior in the underscreened Kondo model *Phys. Rev.* B **68** 220405

[126] Posazhennikova A, Bayani B and Coleman P 2007 Conductance of a spin-1 quantum dot: the two-stage Kondo effect *Phys. Rev.* B **75** 245329

[127] Surer B, Troyer M, Werner Ph, Wehling T O, Läuchli A M, Wilhelm A and Lichtenstein A I 2012 Multiorbital Kondo physics of Co in Cu hosts *Phys. Rev.* B **85** 085114

[128] Biermann S, Aryasetiawan F and Georges A 2003 First principles approach to the electronic structure of strongly correlated systems: combining GW with DMFT *Phys. Rev. Lett.* **90** 086402

[129] Taranto C, Kaltak M, Parragh N, Sangiovanni G, Kresse G, Toschi A and Held K 2013 Comparing quasiparticle GW+DMFT and LDA+DMFT for the test bed material $SrVO_3$ *Phys. Rev.* B **88** 165119

[130] Hansmann P, Ayral T, Vaugier L, Werner P and Biermann S 2013 Long-range coulomb interactions in surface systems: a first-principles description within self-consistently combined GW and dynamical mean-field theory *Phys. Rev. Lett.* **110** 166401